Title: Conjunctive spatial and idiothetic codes are topographically organized in the lateral septum

Authors: Suzanne van der Veldt[1*], Guillaume Etter[1], Fernanda Sosa[1], Coralie-Anne Mosser[1], Sylvain Williams[1*]

[1] McGill University & Douglas Mental Health University Institute, Montreal, Canada
6875, Boul. LaSalle, Verdun (Quebec), H4H 1R3, Phone: 514 761-6131, Fax: 514 888-4067
*Corresponding authors

Abstract

The relevance of the hippocampal spatial code for downstream neuronal populations – in particular its main subcortical output, the lateral septum (LS) - is still poorly understood. Here, we addressed this knowledge gap by first clarifying the organization of LS afferents and efferents via retrograde and anterograde trans-synaptic tracing. We found that mouse LS receives inputs from hippocampal subregions CA1, CA3, and subiculum, and in turn projects directly to the lateral hypothalamus (LH), ventral tegmental area (VTA), and medial septum (MS). Next, we functionally characterized the spatial tuning properties of LS GABAergic cells, the principal cells composing the LS, via calcium imaging combined with unbiased analytical methods. We identified a significant number of cells that are modulated by place (38.01%), speed (23.71%), acceleration (27.84%), and head-direction (23.09%), and conjunctions of these properties, with spatial tuning comparable to hippocampal CA1 and CA3 place cells. Bayesian decoding of position on the basis of LS place cells accurately reflected the location of the animal. The distributions of cells exhibiting these properties formed gradients along the anterior-posterior axis of the LS, directly reflecting the

organization of hippocampal inputs to the LS. A portion of LS place cells showed stable fields over the course of multiple days, potentially reflecting long-term episodic memory. Together, our findings demonstrate that the LS accurately and robustly represents spatial and idiothetic information and is uniquely positioned to relay this information from the hippocampus to the VTA, LH, and MS, thus occupying a key position within this distributed spatial memory network.

Keywords: Lateral septum, spatial navigation, calcium imaging, place fields, head direction

Introduction

The lateral septum (LS) is an anatomically complex structure uniquely positioned within a broader distributed spatial memory network. Centrally located in the coronal plane encapsulated by the lateral ventricles[1], the LS consists almost exclusively of highly interconnected GABAergic cells[2]. Previous research has implicated the LS as mediating a wide variety of behaviors, including spatial and working memory tasks[3–7], the regulation of feeding[8–11], anxiety[12–15], locomotion[16,17], and social behaviors[18–21]. Despite this diversity of implicated behaviors, functional characterizations of the LS have often focused on the spatial coding properties of these neurons, primarily due to the extensive excitatory input from positionally-tuned hippocampal pyramidal neurons often referred to as 'place cells'[21–24].

This work has not yet yielded a consensus. Several studies have reported place cells in the LS, but the number, information content, and stability vary widely from study to study[17,25–29], while others described a lack of canonical place cells[24]. As previous studies often depended on variable criteria of what defines a place cell, estimates range from 5.3%[24] to 56.0%[17] of LS cells classified as spatially-modulated. Strikingly, even estimates by the same authors on data acquired from the same subjects engaging the same task ranged

between 26.5%[30] to 56.0%[17]. When reported, LS place cells are typically described as of lesser quality than classic hippocampal place cells, with lower within-session stability and larger place fields[28,29]. In addition to rate-coding place cells, recent evidence suggests that the LS may integrate the animal's position in space through a phase-code inherited from sequences of CA3 and CA1 place cell assemblies[24,31]. Adding to this complexity, the LS is a large structure that is cytoarchitecturally subdivided into dorsal, intermediate, and ventral subregions spread across its anterior-posterior axis[22,23], suggesting that the striking differences in LS spatial coding characteristics between studies may be in part a product of variations in recording locations within the region. In addition to position, LS neurons may also encode other spatial variables such as acceleration, velocity, and direction[17,28,29].

Beyond their basic spatial tuning properties, hippocampal place cells are also noted for the rapid reorganization of the place fields across time (on the order of days) and navigational contexts, a phenomenon termed remapping[32–36]. If the LS spatial code is inherited from its hippocampal inputs, one would expect comparable dynamics over a similar timescale. In contrast, the LS has been implicated in behaviors that may require a stable representation of space over time, including context-reward[37,38], contextual fear conditioning[13,39–42] and spatial learning and memory[30,43,44]. Thus whether and how the LS spatial code changes across time is crucial to clarifying its relationship to the upstream hippocampal spatial code, with important implications for its involvement in this broader spatial memory network as well as how it supports behaviors across longer timescales.

To resolve these outstanding questions, we first characterize the organization of LS inputs and outputs along the anterior-posterior and dorsal-ventral axes via retrograde and anterograde trans-synaptic tracing using rabies and AAV1, respectively. Next, we functionally characterize the spatial coding properties of LS neurons across the anterior-posterior and dorsal-ventral axes. To this end, we recorded ~2000 LS neurons using head-

mounted miniaturized microscopes in awake and freely-behaving mice navigating in linear track and open field environments. Results demonstrate that the LS accurately and robustly represents spatial, speed, and directional information in an anatomically-organized fashion.

Results

The lateral septum as a core node within a distributed network

To assess the distribution of excitatory pyramidal inputs from each hippocampal subregion to the GABAergic cells of the LS, we injected a monosynaptic retrograde rabies tracer in the LS (Fig. 1a, n = 5 mice). The majority of starter cells (rabies-mCherry$^{+,}$ TVA-oG-eGFP+ cells) were located in the dorsal portion of the LS (Fig. 1b). We observed strong labeling of pyramidal neurons of the hippocampus in both hemispheres (Fig. 1c) at both dorsal and ventral levels (Fig. 1d). Interestingly, only the deep portion of CA1 along the radial axis was labeled, suggesting the existence of a distinct HPC-LS sub-circuit. We quantified the distribution of pyramidal cells along the anterior-posterior axis, comparing the average number of rabies-mCherry positive cell bodies per 300µm coronal section at the level of the subiculum, CA1, CA2, CA3, and fasciola cinereum (FC) (Fig. 1e). In the dorsal hippocampus, most pyramidal cells projecting to the LS originated in CA3 (Fig. 1f). At more posterior levels of the hippocampus, LS inputs from CA1 and CA3 were similar (Fig. 1f). Neurons of the dentate gyrus were not labeled. Other significant sources of inputs to LS were the VTA (Fig. 1g), the LH (Fig. 1h), and the periaqueductal grey (PAG, Fig. 1i).

Next, we determined the direct projection targets of the GABAergic neurons of the LS using a Cre-dependent anterograde tracer injected in the dorsal LS of a VGAT-Cre mouse (Supplemental Fig. 1) and observed eYFP-positive axons at the level of the MS, LH and VTA (Supplemental Fig. 1c-e). The dorsal LS was not found to project back to the hippocampus (Supplemental Fig. 1f,g) directly. The projections to the VTA constitute a

bidirectional network, with dopaminergic projections originating in the VTA targeting only intermediate LS, and GABAergic fibers from LS targeting VTA (Supplemental Fig. 2).

To map out the mono- and disynaptic connections between hippocampal and LS neurons, we transfected an anterograde transsynaptic Cre-expressing AAV1 viral vector [45], in either the dorsal CA1 (dCA1) or dorsal CA3 (dCA3, Fig. 2a,b). We subsequently injected a Cre-dependent eYFP expressing virus in the LS to visualize cells that receive direct hippocampal input (Fig. 2a-c). Importantly, this approach allowed us to quantify the cells along the LS anterior-posterior and dorsal-ventral axis receiving direct hippocampal inputs, and assess the density of their distribution within the anterior regions of the LS (+1.0 to 0.0 anterior-posterior). Both dorsal dCA1 and dCA3 injections resulted in the strongest transfection of LS cell bodies in dorsal regions compared to intermediate and ventral LS (Fig. 2d-f). Hence, the density of hippocampal innervation to the LS is a gradient along the dorsal-ventral and anterior-posterior axis, with dorsal-posterior LS neurons receiving more substantial dorsal hippocampal inputs.

As our transsynaptic tracing approach allowed us to determine whether these downstream targets of the LS were part of a direct hippocampus-LS circuit, we investigated the second-order targets of the dorsal CA1-lateral septum (dCA1-LS) and dorsal CA3-LS (dCA3-LS) projections. For either dCA1 or dCA3 injections, we observed a direct disynaptic pathway from the hippocampus to the hypothalamic regions (Fig. 2g). We observed that dCA1-LS preferentially targets the LH, and dCA3-LS targets the hypothalamus more broadly as well as the nuclei of the medial zone. Strikingly, we found eGFP positive fibers again at the level of the medial septum (Fig. 2h). In order to determine whether the projections observed at the level of the LS with both our anterograde tracing approaches constituted passing fibers or synaptic connections, we used an AAV-Flex-Synaptag[46], a Cre-dependent viral construct to express mRuby in the cytosol and eGFP bound to synaptophysin, a protein

primarily expressed in the presynaptic endings of cells participating in synaptic transmission (Fig. 2i). We transfected cells at the level of the dorsal LS and observed significant synaptophysin-bound projections in the medial septum (Fig. 2j), confirming the existence of direct, functional projections to medial septum neurons. Together, our tracing approaches show that LS receives direct inputs from CA1, CA2, CA3, the subiculum as well as the VTA, and in turn projects to the medial septum, VTA, and the hypothalamus (Fig. 2k, Supplemental Fig. 1, Supplemental Fig. 2).

LS GABAergic neurons exhibit stable spatial activity during free exploration

Previous electrophysiological studies of the LS disagree on both the number of place encoding cells and their spatial content. We hypothesize that LS place cell properties vary with recording location within the region. To investigate the spatial coding properties of the LS, we expressed the calcium (Ca^{2+}) indicator GCaMP6f in the GABAergic cells of the LS of mice (Fig. 3a). We recorded Ca^{2+} activity of 1899 neurons in 28 mice implanted in distinct subregions of the LS, while the animals were freely exploring a novel open field. We subsequently filtered and binarized the recorded calcium traces (Fig. 3b)[47] and excluded periods of immobility ($< 5 cm.s^{-1}$). We found that LS GABAergic activity was significantly spatially modulated (Fig. 3c,d) in comparison to circularly shuffled surrogates ($p < .01$, Fig. 3e). To assess the stability of the spatial coding, a within-session stability score was computed for each cell (Fig. 3f). Using an information-theoretic framework [48–50], we computed the mutual information (MI) between calcium activity and spatial location for each cell and expressed the results in bits [47]. To circumvent the inherent issue of sparse sampling in 15min long recordings, we computed the mean MI and confidence interval using 30 bootstrap samples (50% data sampling per sample, Fig. 3g). LS cells were ranked using the distance between their actual MI versus that of the corresponding shuffled surrogates (Fig.

3g,h, Supplemental Fig. 3). Out of 1889 recorded cells, 38.01% (718/1889) of LS cells displayed significant spatial information ($p < .01$; Fig. 3j,k). Despite the known involvement of the LS in feeding-related behaviors, we did not observe any increased number of place cells with fields around food zones, nor did we observe overrepresentation of objects or walls (Supplemental Fig. 4). With theta-rhythmic cells in the LS having higher firing rates than theta-rhythm independent cells[51], we asked whether LS cells with higher firing rates were also more likely to be spatially modulated. Spatially-modulated cells were significantly more active than non-modulated cells (Mann-Whitney test, U = 342219, $p < .0001$; Fig. 3m) and displayed a higher bursting index, defined as the probability of a cell being active, given it was already in an active state, or p(a|a), than non spatially modulated cells (Mann-Whitney test, U = 36876, $p < .0001$; Fig. 3m).

Previous studies have used decoding methods to predict behavioral variables from calcium imaging data recorded in the hippocampus[32,36,52], yielding insights into the amount of information encoded by a neuronal assembly. Here, we asked whether we could reliably estimate the mouse location solely from LS neuronal activity patterns. To assess decoding accuracy, we computed the mean decoding error and mean decoding accuracy (Fig. 3n-p, see Methods). In the open field, decoding using LS activity significantly outperformed a decoder that was trained using shuffled data (mean decoding error: paired t-test, $t(5) = 4.883$, $p = .0045$, Fig. 3q; mean decoding agreement: paired t-test, $t(5) = 4.698$, $p = 0.0053$, Fig. 3r, Supplemental Fig. 5a) even when decreasing the number of neurons used to only 40 neurons, for both decoding error (two-way repeated-measures (RM) ANOVA, $F(3,19) = 571.4$, $p = 0.0024$ for main effect of shuffle, $F(3,19) = 6.948$, $p = 0.0024$ for main effect of number of included cells; Supplemental Fig. 5a) and decoding agreement (two-way RM ANOVA, $F(3,19) = 1059$, $p < .0001$ for main effect of shuffle, $F(3,19) = 10.06$, $p = 0.0003$ for main effect of number of included cells; Supplemental Fig. 5a).

Next, it was determined whether LS place cells had spatial properties that were dependent on the localization of their recording. To measure this, we classified the location of GRIN lens implants along the dorsal-ventral and anterior-posterior axis (Supplemental Fig. 3s, Supplemental Fig. 6). Post-mortem histological verification of GRIN lens implant combined with within-animal analysis of the location of recorded cells enabled us to approximate the location of each recorded cell (Fig. 3t). While we observed no differences in cell activity characteristics, such as bursting index or activity probability along the anterior-posterior axis, medial-lateral or dorsal-ventral axis (Supplemental Fig. 7), we found a pronounced increase in the portion of stable place cells (within-session stability > .5) along the anterior-posterior axis (linear regression, $R^2 = 0.1272$, $p = 0.013$, the proportion of stable cells per 0.2 mm bin per animal, n = 24 mice, Fig. 3u). On the other hand, we observed a similar gradient along the dorsal-ventral axis, with a larger proportion of stable place cells found at the more dorsal regions of the LS, although this trend failed to reach significance (linear regression, $R^2 = 0.129$, $p = .0848$, n = 24 mice; Fig. 3v). Taken together, these data strongly suggest that regions of the LS that receive stronger innervation from the dorsal hippocampus have a larger proportion of cells that reliably encode space; thus it likely that this information is directly inherited from the hippocampus.

LS conjunctive coding for directionality, velocity, and acceleration

In CA1, place cells have been found to carry directional[53–55] and speed-related information[56,57], with speed found to be selectively encoded by inhibitory interneurons[58]. Previous studies found that subsets of LS neurons show some degree of modulation by locomotion direction[29] as well as velocity and acceleration[17] through correlative measures in spatial alternation or t-maze navigation tasks, where the relationship between cell activity patterns and movement-associated variables may be confounded with task-dependent

variables. Here, we again employed an information-theoretic approach to compute the MI between calcium activity and each of these correlates in a free foraging task in the open field. We found that 23.09% (388/1442) of LS cells are significantly modulated by head direction (Fig. 4a-d, Supplemental Fig. 8), velocity (23.71%, 448/1889, Fig. 4e-h), or acceleration (27.84%, 526/1889, Fig. 4i-l). Given the relatively large population of LS cells selective for these covariates, we assessed conjunctive coding in the LS. We found cells that were significantly tuned to more than one of these variables (Fig 4m,n), with 30.97% of cells (381/1230) encoding more than one modality (Fig. 4o). Of these conjunctive cells, cells that encode both place and head direction are most abundant (94/1230). Contrary to previous reports[17], cells that encode both velocity and acceleration but not place or HD were found to be sparse in the LS (11/1230). Together, this conjunctive coding for location, directionality, and velocity parameters indicates that LS cells fire in response to more complex navigational features.

We also assessed the topographical distribution of these head direction, velocity and acceleration tuned cells within the LS. We observed a pronounced dorsal-ventral gradient in the distribution of stable (within-session stability > .5) head direction cells (linear regression, R2 = 0.3837 p = 0.0061, n = 17 mice, Fig. 4p), with most directionally modulated cells located at the more dorsal regions of the LS, but we did not observe such a gradient along the anterior-posterior axis (linear regression, R2 = 0.014, p = .3542, n = 24 mice; Fig. 4p). Velocity modulated cells were mostly found at the ventral pole of the LS (linear regression, R2 = 0.1836, p = 0.0367, n = 24), but no such gradient was found along the anterior-posterior axis (linear regression, R2 = .0075, p = .4481, n = 24). Acceleration-modulated cells were found evenly distributed throughout the LS (DV: R2 = .0146, p = .2928; AP: R2 = .00055, p = .7981, n = 24 mice). Lastly, we investigated decoding error and agreement for head direction: even with relatively large decoding errors, decoding using LS neuronal data was

significantly better than a shuffled dataset (mean decoding error: paired t-test, t(3) = 7.699, *p* = .0046, Fig. 4q; mean decoding agreement: paired t-test, t(3) = 15.62, *p* = 0.0006, Fig. 4q, Supplemental Fig. 5c).

LS place cells share characteristics with CA1 and CA3 place cells

We next compared the place field properties of cells recorded in LS to those of place cells recorded in CA1 and CA3 as a benchmark using the same recording method (Fig. 5a,b). For each animal, we computed the portion of significantly positionally modulated cells per region, which was not significantly different across LS, dCA1, and dCA3 (one-way ANOVA, F(2,34) = 0.499, *p* = .6110, Fig. 5c). As expected on the basis or prior results[24,26,28,29], the within-session stability of LS cells was significantly lower than that of place cells recorded in CA1 and CA3 (Kruskal-Wallis, H(3) = 49.44, *p* < .0001; Fig. 5d). Conversely, the activity of LS neurons was significantly higher than those of dCA1 and dCA3 principal cells (Kruskall-Wallis, H(3) = 56.76, *p* < .0001; Fig. 5e), and place fields were more dispersed (Kruskall-Wallis, H(3) = 93.21, *p* < .0001, Fig. 5f). When decoding the location of the animals using a bootstrapped sample of 80 cells from each region, the decoder trained on data from LS performs significantly worse than a decoder using CA1 data (mean decoding agreement: Kruskall-Wallis, H(3) = 8.211, p = .0024, Fig. 5g). Decoding error was numerically higher in the LS than CA3 as well, though this difference did not reach significance (mean decoding error: Kruskall-Wallis, H(3) = 5.635, p = .0364, Fig. 5g).

In contrast to their omnidirectional firing properties in open field environments, hippocampal neurons rapidly develop strong directional selectivity in linear tracks[57,59,60]. To test whether the LS place code developed comparable directional selectivity, we next recorded from either LS, CA3, or CA1 neurons while mice ran on a linear track (Fig. 6a). In well-trained LS animals, we recorded 490 place cells (45.29%, n = 1082 cells, n = 15 mice,

Fig. 6b-d). Within-session stability of spatially modulated cells was higher than for those that were not significantly spatially modulated (Wilcoxon test, $p < .0001$, Fig. 6d). As shown in the open field, decoding using LS neuronal activity of mice running on the linear track significantly outperformed a decoder that was trained using shuffled data (mean decoding error: paired t-test, $t(3) = 16.16$, $p = .0005$, Fig. 6g; mean decoding agreement: paired t-test, $t(3) = 14.27$, $p = 0.0007$, Fig. 6h), even when decreasing the number of neurons used, for both decoding error (two-way RM ANOVA, $F(3,19) = 571.4$, $p = 0.0024$ for main effect of shuffle, $F(3,19) = 6.948$, $p = 0.0024$ for main effect of number of included cells; Supplemental Fig. 5b) and decoding agreement (two-way RM ANOVA, $F(3,19) = 1059$, $p < .0001$ for main effect of shuffle, $F(3,19) = 10.06$, $p = 0.0003$ for main effect of number of included cells; Supplemental Fig. 5b). We next set out to compare LS and hippocampal place cell characteristics in the linear track (Fig. 6i). We found that even though within-session stability of place cells was significantly different between LS, dCA1, and dCA3, stability in the LS was not significantly different than in dorsal CA1 (Kruskall-Wallis, $H(3) = 8.922$, $p = .0116$, Fig. 6k). Overall, place cells recorded in LS were significantly more active than those recorded in the hippocampus ($H(3) = 155.1$, $p < .0001$, Fig. 6k). Similar to hippocampal cells, we found directionally modulated cells in the LS (Fig. 6i-o). By ranking place cells as a function of the difference between left and right MI (Fig. 6o), we found cells tuned to the absolute location regardless of direction (83/1082, 7.67%), while other cells were selective to the left- (168/1082, 15.52%), or right-trajectories (239/1082, 22.08%). Some cells were not significantly modulated by space (592/1082, 54,71%, Fig. 6p).

A subset of LS cells has stable spatial representations up to 8 days

To test whether the LS and the hippocampus exhibit comparable evolutions of their spatial code over time, we recorded from CA1 and LS neurons in a novel open field over both

short (3 days) and longer timescales (8 days, Fig. 7a). We assessed the stability of the spatial map across sessions, and we observed a subset of LS place cells that were stable over time (Fig. 7b). Correlating the tuning maps of aligned LS cell pairs over days lead to a significant increase in correlation value over days (two-way ANOVA, $F(2, 1470) = 8.129$, $p = 0.0003$, the main effect of time) with LS cells being statistically more stable than shuffled comparisons ($F(2,1470) = 197.3$, $p < .0001$, main effect of shuffle, Fig. 7c). There was no significant increase in the proportion of place cells per animal over days (one-way ANOVA, $F(3,16) = 1.618$, $p = .2247$, Fig. 7d). We observed the strongest within-session stability on day 3 (Kruskal-Wallis, $H(4) = 19.16$, $p = 0.0003$; Fig. 7e), as well as a steady increase in spatial information (Kruskal-Wallis, $H(4) = 13.27$, $p = 0.0041$; Fig. 7f). We computed the mean stability for each place cell pair recorded over multiple days (Fig. 7g), and when comparing the mean tuning map correlation between day 1 and 8 for LS and CA1 place cells, we found no significant difference in their stability (unpaired t-test, $t(68) = 1.475$, $p = 0.1449$, Fig. 7h). Together, this suggests that a subset of LS cells codes for space over longer periods of time, similarly to what has been described for CA1[32,36].

Discussion

Here, we found an anterior-posterior and dorsal-ventral gradient in the density of dorsal hippocampal inputs to the LS, with the strongest hippocampal innervation at the more dorsal-posterior levels of the LS. While spatial coding has been extensively characterized in the hippocampal formation, how downstream regions process this information has only more recently begun to receive attention. The LS has re-emerged as a critical region implicated in a space encoding network, although electrophysiological recordings of the LS in rats have led to disparate estimates of the quantity and quality of place cells in the region[17,26,30]. Strikingly, LS place cells recorded on a circular track described to be almost absent [24], but found to be

abundant in reward-seeking tasks[17,30]. Using calcium imaging and unbiased information metric and decoding approaches, we found that 38.01% of GABAergic LS cells robustly code for space during free exploration in an open field and 45.29% of cells during linear track alternation. In addition to spatial information, we found that the LS also reliably encodes velocity (23.71%), acceleration (27.84%), and head direction (23.09%). with conjunctive coding being abundant, suggesting that the LS encodes more complex navigational features than previously thought. This may be partially due to the high convergence of hippocampal efferents onto LS neurons, which has been described to be 20-800 times more dense than any cortical targets[24].

Tracing work done in rats showed that these hippocampal neurons project to the LS in a precise topographical order with CA1 and subiculum projecting rostrally and exclusively unilaterally, whereas CA3 projections target the more posterior, lateral part of the LS[23,61]. Using transsynaptic anterograde tracing, we found a dorsal-ventral and anterior-posterior gradient in the density of dorsal hippocampal inputs in line with previous work in the rat [23]. The LS, in turn, provides regions located downstream of the hippocampus with positional and idiothetic information, as we found that LS cells receiving hippocampal inputs in turn project directly to the LH and the MS. Although the existence of an LS-MS projection has long been debated[23,62–65], we observed labeling at the level of the MS after transfection of dCA1-input and dCA3-input receiving LS cells. The MS plays a well-described neural role in generating and propagating theta rhythms throughout the hippocampal formation[66–68], which in turn organizes hippocampal place cell activity[69], as well as a behavioral role in the initiation and velocity of locomotion[70,71]. A functional role of the LS within this hippocampal-LS-MS circuit has been suggested previously, through the effects of LS inhibition or activation on MS theta rhythmicity[19,51] and the regulation of running speed[16]. Moreover, we observed a direct projection from the LS to the hypothalamus, a highly connected region traditionally

known as necessary for the regulation of feeding[72], arousal and motivation[73], and more recently learning and memory[74–77]. The LH is crucial for the control of locomotion[78–81] and thought to mediate motivational and goal-directed processes underlying feeding[9,72,82,83]. This microcircuit – from principal hippocampal cells, via spatially modulated LS cells, to the MS and LH - is of particular interest, as both the MS and LH do not appear to receive direct inputs from the principal hippocampal cells themselves. As a core node within this network, the LS may be important for the translation of spatial information to goal-directed or environmentally appropriate actions necessary for survival. Despite this interconnectedness with the LH and previous reports of LS place cells being skewed towards reward in a spatial navigation task[30], we did not observe any increased LS place cell overrepresentation around food zones during free exploration.

Here we found a significant proportion of LS cells to reliably code for space while the animal was freely exploring a novel open field. Previous work has hinted at a dorsal to ventral organization of the LS place code: electrophysiology studies recorded a slightly larger proportion of LS place cells in the more dorsal regions[28]. A complementary anatomical microstructure has been previously described for the rate-independent phase code in the LS, where the strength of the phase code increased as a function of recording depth along the dorsal-ventral axis[84]. Here we find that lateral septal place cells are arranged along an anterior-posterior gradient similar to the gradient of hippocampal inputs into the LS – a finding that helps to reconcile the variation in previously reported estimates of LS place cell prevalence, which ranged between 5.3% of cells recorded along the dorsal-ventral axis[24] up to 56% recorded at the most dorsal level of the LS[17]. This pattern suggests that the inhibitory neurons of the LS may inherit a place code from the hippocampus, with subregions receiving dorsal hippocampal inputs being most similar to the classical hippocampal place cells.

Surprisingly, we found that the majority of CA1 pyramidal inputs to LS originated in the deep layer, which could support a sub-circuit distinct from superficial CA1[85]. Previous work has shown that superficial and deep CA1 pyramidal cells comprise two distinct sublayers, characterized by differential inputs from the entorhinal cortex and CA2[86]. Place cells found in the deep layer were preferentially stable during goal-oriented learning, with the representation of the reward zone by deep cells predicting task performance[85,86], similar to some of the reported properties of dorsal LS cells[30]. As our viral tracing shows that the dopaminergic cells of the VTA project solely to the intermediate LS, with projections to dorsal LS virtually absent, information about reward location is more likely inherited from hippocampal reward cells[87] than from the dopaminergic neurons of the VTA.

In addition to place cells, we observed significant proportions of velocity and acceleration modulated cells. These cells have been previously described by others using correlative measures, although estimated proportions vary widely: for velocity tuning in reward-seeking tasks, estimates range from almost absent[84], to almost 60% of cells[17]. For acceleration, approximately 45% of LS cells have been found to show some degree of correlation, with almost 30% of recorded cells correlated with both speed and acceleration[17]. Here, using information metrics and a free exploration task in which firing characteristics are less easily confounded with task parameters, we find that 23.71% of LS GABAergic cells are modulated by velocity, and 27.84% of cells modulated by acceleration. Despite conjunctive coding being abundant in the LS (30.97%), cells coding for both velocity and acceleration were found to be sparse (<1%). Velocity and acceleration cells were distributed dissimilarly in the LS, with velocity cells being more abundant towards the ventral pole, whereas acceleration modulated cells were found to be distributed equally. This raises the question whether velocity and acceleration information are inherited from different areas upstream of the LS. Interestingly, head direction was more abundant towards the dorsal portion of the LS

but distributed equally along the anterior-posterior axis. Previous studies have identified HD cells in multiple, well-described circuits, including the postsubiculum[88], anterodorsal thalamic nucleus[89], mammillary bodies[90], and entorhinal cortex[91]. A probable source of directional information to the LS is the entorhinal cortex (Allen Brain Connectivity Atlas, Oh et al., 2014)

Our work supports the perspective that LS neurons combine a wide range of modalities and may form a complex representation of context over longer timescales than previously reported. Neuronal representations in the hippocampus have been found to change over time, with place code ensembles changing rapidly: an estimated ~40%[32] to ~75-85%[36] of CA1 neurons were found to remap over days. In the posterior LS, we found a subpopulation of cells that display stability over eight days, comparable to CA1 cells recorded under the same conditions. The functional role of such stability remains to be elucidated. One possibility is that this ensemble may mediate the stable encoding of contexts over longer durations of time, which could account for the critical importance of the LS for a number of behaviors that appear to require a stable representation of the spatial map, including contextual fear conditioning[13,39–42], context-reward associations[38,93] and radial-maze navigation tasks[43,44]. In addition to space, velocity and reward information, hippocampal pyramidal cells have been shown to encode variables such as time[94,95], odor[96,97] and sound frequency[98]. Whether this information is also relayed to the LS remains to be elucidated.

In summary, we have shown that the GABAergic cells of the LS may provide the VTA, LH, and MS with information about location, direction, and speed, and therefore constitute a core node within a distributed spatial memory network. Within this network, the LS may be important for the translation of spatial information to goal-directed or environmentally appropriate actions necessary for survival.

Methods

Animals

All procedures were approved by the McGill University and Douglas Hospital Research Centre Animal Use and Care Committee and in accordance with the Canadian Council on Animal Care. Naive mice (C57Bl/6, Charles River; Vgat-ires-Cre, The Jackson Laboratory) were housed individually on a 12-hour light/dark cycle at 22°C and 40% humidity with food and water ad libitum. All experiments were carried out during the light portion of the light/dark cycle. Both male and female mice were used for this study.

Virus injections

Mice, 8-16 weeks old, were anesthetized with isoflurane (5% induction, 0.5-2% maintenance) and placed in a stereotaxic frame (David Kopf Instruments). Body temperature was maintained with a heating pad, and eyes were hydrated with gel (Optixcare). Carprofen (10 ml/kg) was administered subcutaneously. All viral injections were performed using a glass pipette connected to a Nanoject III (Drummond) injector at a flow rate of 1 nL/second, at the following coordinates (Anterior LS: anterioposterior (AP): +0.86 , mediolateral (ML): +0.35 , dorsoventral (DV): -3.0; Intermediate LS: AP: +0.38, ML: +0.35; DV: -2.7, Posterior LS, AP: +.10, ML: +.35; DV: -2.5, with DV + or - .2 to adjust for dorsal, ventral or intermediate; CA1, AP: -1.86 mm, ML: 1.5 mm, DV: 1.5 mm; CA3, AP: -2.1, ML: 2.3; DV: 2.2) All stereotaxic coordinates are taken from Bregma. After surgery, animals were continuously monitored until recovery. For three days after surgery, mice were provided with a soft diet supplemented with Carprofen for pain management (MediGel CPF, ~5mg/kg/day).

Retrograde tracing studies were done using a Cre-dependent retrograde Rabies tracing approach. Briefly, 100 nL of helper virus (AAVdj.hSyn.Flex.TVA.P2A.eGFP.2A.oG, NeuroPhotonics Center, Laval, Canada, Wickersham et al., 2007, Callaway, 2008) was injected in the LSd (coordinates as above) of VGAT-ires-Cre transgenic mice (n = 5 animals, Slc32a1$^{tm2(cre)Lowl}$/J, JAX stock #016962). Cre specificity was tested by the NeuroPhotonics center. After 4 weeks of incubation time to allow for the complete expression of the helper virus, 200 nL of inactivated EnvA pseudotyped rabies virus coupled to mCherry was injected (RABV-EnvA-deltaG-mCherry, NeuroPhotonics Center) at the same coordinates, and brains were collected 7 days later.

Cell type unspecific retrograde tracing was done using cholera toxin β-subunit (CTB) conjugated to Alexa 647 (Thermofisher, C34778), using a unilateral injection of 30 nL targeted at the dorsal LS in N = 4 C57Bl6 animals. Animals were left in their home cage for 7 days before brains were collected and processed as described below.

To distinguish synaptic targets from passing projection fibers of dCA1 and dCA3 within the LS, animals received a bilateral injection of transsynaptic Cre-inducing anterograde virus (AAV1-hSyn-Cre-WPRE-hGH, Penn Vector Core via Addgene, V24784) mixed with a Cre-dependent tdTom reporter virus to visualize injection sites (AAV2-Ef1a-flex-tdTomato, NeuroPhotonics Center, Laval, Canada, AAV602) in a 3:1 ratio, 80 nL total injection volume per hemisphere (n = 5 C57Bl6 animals per group). After 1 week of incubation time, this was followed up by bilateral injection of a Cre-dependent anterograde vector in LS expressing enhanced yellow fluorescent protein (400 nL, bilateral, AP: 0.5, ML: 0.35, DV: 2.6, AAVdj-DIO-Cheta-eYFP, NeuroPhotonics Center, AAV938). After three weeks, brains were collected and processed.

To verify that synaptic connections were present at the level of the LS-MS projection, AAVdj-hSyn-flex-mRuby2-syp-eGFP construct (NeuroPhotonics Center, AAV799) was

injected in the LS of CAMKII-cre mice (B6.Cg-Tg(Camk2a-cre)T29-1Stl/J), with 100 nL total injection volume injected at 1 nL/second. After 4 weeks of incubation time, animals were perfused, and brains were processed as described below.

GRIN lens implant and baseplate

Two to four weeks post-injection, a 0.5 mm diameter gradient refractive index (GRIN, Inscopix) lens was implanted above LS, dorsal CA1 or CA3, or a 1.8 mm GRIN (Edmund Optics) lens was implanted above dorsal CA1. For .5 mm lens implant, the lens was glued to an aluminum baseplate prior to the surgery, which provided two main advantages: 1) it allowed us to implant the baseplate/lens assembly in one surgery (instead of separate surgeries) and 2) during the surgery the miniscope was used to image for fluorescence while lowering the lens. The mouse was anesthetized with isoflurane, and the skull was cleared. A ~.6 mm diameter hole was drilled in the skull at the level of the injection site. An anchor screw was placed above the contralateral cerebellum to stabilize the implant. The baseplate and GRIN combination were attached to the miniscope and together secured to the stereotaxic frame. After making a leading track using a .5 mm diameter needle, the implant was lowered in place. While lowering the GRIN lens into the tissue, and a bright fluorescent signal indicates that the injection site has been reached. Both the GRIN lens and baseplate were permanently secured using C&B-Metabond (Patterson Dental). A plastic cap was used to protect the GRIN lens from scratching during the recovery period and in between recording sessions. The animal was given 4 - 6 weeks of recovery time before experiments started. LS implants were targeted at the following coordinates: Anterior LS: anterioposterior (AP): +0.86 , mediolateral (ML): +0.35 , dorsoventral (DV): -2.9; Intermediate LS: AP: +0.38, ML: +0.35; DV: -2.65, Posterior LS, AP: +.10, ML: +.35; DV: -2.45, with DV + or -

.2 to adjust for dorsal, ventral or intermediate; CA3 implants were targeted at AP: -2.1, ML: 2.2; DV: 2.2.

For 1.8 GRIN lens implantation, a ~2 mm diameter hole was perforated in the skull. Again, an anchor screw was used to secure the implant in place. After removing the dura, a portion of the cortex above the injection site was gently aspirated using a vacuum pump without applying pressure on the underlying hippocampus. The 1.8 mm GRIN lens was lowered at the following coordinates: AP -1.86 mm from bregma, ML 1.5 mm, DV 1.2 mm. The GRIN lens was permanently attached to the skull using Metabond, and Kwik-Sil (World Precision Instruments) silicone adhesive was placed on the GRIN to protect it. 4 weeks post-implant, the silicone cap was removed, and CA1 was imaged using a miniscope mounted with an aluminum base plate while the mouse was under light anesthesia (~0.5 % isoflurane) to allow the visualization of cell activity. When a satisfying field of view was found (large number of neurons, visible landmarks), the baseplate was cemented above the GRIN lens and a protective cap was used to protect the GRIN from scratching. Imaging would start ~1 week after base plating.

Miniscope recordings

The mouse was habituated by being gently handled for ~5 min per day for 3 days. The mouse was then water or chow-scheduled (2h access per day). Miniscope recordings performed at 30 Hz for 15 minutes every day, with just one recording session per day to minimize photobleaching. For open field recordings, animals were freely foraging for randomly placed 10% sucrose or 10% sweetened condensed milk in water rewards. The environments consisted of a 45 x 45 cm dark grey open field with visual cues, or a 49 x 49 cm white plexiglass open field, which was placed in different recording chambers. For linear track recordings, rewards (30 ul of 10% sucrose water) were placed at each end of the 100 cm

linear track, or a 130 cm linear track, and the mouse had to consume one reward before getting the next one delivered.

Miniscope and behavior video acquisition

Miniscopes (V3, miniscope.org) were assembled using open-source plans as described previously (Ghosh et al., 2011; Cai et al., 2016). Imaging data were acquired using a CMOS imaging sensor (Aptina, MT9V032) and multiplexed through a lightweight coaxial cable. Data was acquired using a data acquisition (DAQ) box connected via a USB host controller (Cypress, CYUSB3013). Animal behavior was recorded using a webcam mounted above the environment. Calcium and behavioral data were recorded using Miniscope custom acquisition software (miniscope.org). The DAQ simultaneously acquired behavioral and cellular imaging streams at 30 Hz as uncompressed .avi files (1000 frames per file), and all recorded frames were timestamped in order to perform the subsequent alignment.

Histology

After completion of recording experiments, animals were deeply anesthetized with ketamine/xylazine/acepromazide (100, 16, 3 mg/kg, respectively, intraperitoneal injection). Mice were then transcardially perfused with 4% paraformaldehyde in PBS (PFA). Brains were extracted and postfixed in PFA at 4 °C for a minimum of 48 hours. Brains were sectioned at 50 μm using a vibratome and cryoprotected in a solution of 30% ethylene glycol, 30% glycerol and 40% PBS until used.

Immunohistochemistry

Sections were washed 3 x 20 min in PGT (0.45% Gelatin and 0.25% Triton in 1x PBS) at room temperature. Next, primary antibodies (1:1000 goat anti-GFP from Novus Biologicals

or 1:10 000 rabbit anti-RFP from VWR (Rockland) were incubated with PGT overnight at 4°C. Following 10, 20, and 40 min washes in PGT, sections were incubated with secondary antibodies (1:1000 donkey anti-goat coupled to A488 or 1:1000 donkey anti-rabbit coupled to A555, both from Molecular Probes) in PGT at room temperature for 1 hour. Sections were subsequently washed for 10 and 20 minutes in PGT and 30 minutes in PBS. Sections were then mounted on glass slides and permanently coverslipped with Fluoromount that contained DAPI.

Calcium imaging analysis

Calcium imaging videos were analyzed using the Miniscope Analysis pipeline (https://github.com/etterguillaume/MiniscopeAnalysis) as described previously [47,99]. Non-rigid motion correction was applied using NoRMCorre [99], and videos were spatially downsampled (3x) before concatenation. Calcium traces were extracted using CNMFe [100] using the following parameters: gSig = 3 pixels (width of gaussian kernel), gSiz = 20 pixels (approximate neuron diameter), background_model = 'ring', spatial_algorithm = 'hals', min_corr = 0.8 (minimum pixel correlation threshold), min_PNR = 8 (minimum peak-to-noise ratio threshold). After extraction, cells and traces were visually inspected, and cells with low signal to noise ratio were removed. Raw calcium traces were filtered to remove high-frequency fluctuations and binarized (normalized amplitude > 2 sd and the first-order derivative >0).

Position data were inferred offline following the recording, using the red LED on the CMOS of the miniscope. A subset of behavioral videos were analyzed using DeepLabcut through Python Integrated Miniscope Pipeline Notebook (PIMPN, available through https://github.com/etterguillaume/PIMPN) to extract head direction.

Activity and bursting index

Following the binarization of raw calcium traces, we compute the probability of a neuron to be active p(a) using the following formula:

$$P(A) = \frac{time\ active}{total\ time}$$

The bursting index was computed as the probability of a cell being active, given it was already in an active state, or p(a|a). The activity index is computed as the probability of a cell becoming active when it is in an inactive state, or p(a|i).

Spatial modulation

Space was binned (Position in open field: 17 x 17 bins of 3 cm; Position in linear track: 34 bins of 3 cm; velocity, min = 2.5 cm/s, max = 30 cm/s, 20 bins; acceleration: min = -2 cm/s^2, max = +2 cm/s^2, 20 bins; head direction: 24 bins of 15°). Velocity was smoothed over thirty frames to reduce discontinuities. For head direction and positional information, all frames where velocity was < 5cm/s were excluded. The probability of being active P(A) informs on the activity rate of a neuron. Next, we compute the probability of spending time in a given bin *i* (spatial, velocity, acceleration or head direction bin).

$$P(S_i) = \frac{time\ in\ bin\ i}{total\ time}$$

Next, we compute the joint probability:

$$P(S_i \cap A) = \frac{time\ active\ while\ in\ bin\ i}{total\ time}$$

And the probability that a cell is active given the animal is in a bin:

$$P(A \mid S_i) = \frac{time\ active\ while\ in\ bin\ i}{time\ in\ state}$$

After plotting the binarized activity in space, we perform n = 1000 random circular permutations. Circular permutations are used to remove the temporal relationship between

neuronal activity and behavior, but it preserves the temporal structure of calcium transients and therefore leads to more conservative results (as opposed to complete randomization of every data point, which inflates the significance value of results). In this case, the p-value corresponds to the number of datapoints from the shuffled distribution that are greater than the actual data for each bin, divided by the number of permutations [101]. A threshold of $p < .01$ is used to determine the significant data points that make up a significant place field. In our case, for a cell to be considered a place cell, at least one of the spatial bins must contain activity that is significantly non-random. To compute within-session stability, the halfway point in the recording was determined by taking the timestamps where half of the total number of binarized events for the session was reached. Tuning maps were computed for both the first and second half of the session using the methodology described above. A Gaussian smoothing filter ($\sigma = 3$) was used to smooth the tuning maps before computing a correlation between the two. A within-session correlation value of >.5 was considered a stable field.

Calculating mutual information content

Mutual information is used to describe the amount of information about one variable (spatial location, head direction, velocity or acceleration) through the observation of neuronal activity, and was calculated using the following formula:

$$MI = \sum_{i=1}^{M} \sum_{j=1}^{2} P(S_i \cap A_j) \times log2\left(\frac{P(S_i \cap A_j)}{P(S_i) \times P(A_j)}\right)$$

Where M is the total number of possible behavioral states, $P(S_i \cap A_j)$ is the joint probability of the animal being in bin i concurrently with activity level j. As we are using binarized activity, j can only be active or inactive. MI was calculated using 30 bootstrapped surrogates using 50 percent of the data (randomly chosen data points) with replacement, to allow for computation of mean MI and SEM. Next, the trace was circularly shuffled in order to calculate a shuffled

MI and SEM. Cells were then sorted along with the magnitude of the difference between mean MI and mean shuffled MI, and a two-way ANOVA with a $p < .01$ threshold was used to determine whether the difference between the two numbers was significant in order for the cell to be deemed a significant place cell.

Bayesian decoding

A Bayesian decoder was used to evaluate how well LS neural activity estimated the animal's location. We used decoding methods specifically adapted for calcium imaging data with binarized calcium transients [47]. The training dataset was generated using 50% of the data, randomly chosen, using 30 bootstrap samples including 40, 60, 80 or 100 randomly chosen cells (Supplemental Fig. 5). The posterior probability density function, which is the probability that an animal is in a particular bin S_i , given the neural activity A is calculated using the following equation:

$$P(S_i \mid A) = \frac{P\ (A \mid S_i)\ \times\ P\ (S_i)}{P\ (A)}$$

P(S|A) is the posterior probability distribution of states given neuronal activity. No prior assumption is made about the location of the mouse on the linear track, P(S) is kept uniform to attribute equal probability for each location. Every neuron is assumed to be independent of each other. To construct the tuning curves from multiple neurons, we use the following equation:

$$P\ (S \mid A) = \prod_{k\,=\,1}^{N} \frac{P(A_k \mid S)\ \times\ P\ (S)}{P\ (A_k)}$$

With *P(S|A)* a vector of *a posteriori* behavioral states and *N* corresponding to the number of neurons used. For every neuron *k* the tuning curves are constructed, and corresponding posterior location probability can be derived.

To reconstruct the position of the mouse, we will consider the location associated with the maximum a posteriori:

$$\hat{y} = arg\ max\ exp\left[\sum_{k=1}^{N} log\left(1 + \frac{P(A_k \mid S) \times P(S)}{P(A_k)}\right) - 1\right]$$

With the estimated state among all possible states S. We used a temporal filtering window in the open field of 1.5 seconds and in the linear track of 0.5 seconds to remove erratic jumps in the decoded position of the mouse. Decoding accuracy was measured as 1) decoding error and 2) decoding agreement. In one-dimensional space, decoding error was assessed as

$$decoding\ error = |\ decoded\ position - actual\ position\ |$$

In two-dimensional space, decoding error was assessed as

$$decoding\ error = \left(\sqrt{actual\ position - decoded\ position}\right)^2$$

For head direction decoding, the decoding error was the smallest difference in degrees between decoded head direction and actual head direction. Decoding agreement was defined as the portion of time where the exact location or head direction bin was successfully decoded:

$$decoding\ agreement = \frac{time\ points\ successfully\ decoded}{total\ time}$$

Tracking cells across sessions

Neurons were tracked over multiple days using a probabilistic method as previously described [102]. Briefly, spatial footprints were aligned using non-rigid alignment (transformation smoothness = 2) to correct for displacements of the brain or miniscope placement. After alignment, we considered candidate sets of cells to be the same neuron if their maximal distance was < 12 um, and the spatial correlation between sets of cells was > .65. Next, we visually identified candidate cell pairs across sessions and manually deleted those cell pairs that were erroneously selected (< 1% of cases). We assessed the stability of

the spatial representation in LS using two main metrics 1) field correlation and 2) population vector correlation. Field correlation was assessed by correlating smoothed place fields of cell pairs. To generate the null hypothesis for place fields' displacements between pairs of days, we used the place fields tuning maps but shuffled cells identities over days (30 shuffles).

Materials availability

This study did not generate new unique reagents.

Data and Code availability

All data will be made publicly available. Code for cell extraction is available at https://github.com/etterguillaume/MiniscopeAnalysis. Code for behavior extraction is available at https://github.com/etterguillaume/PIMPN. Code for extraction of tuning curves and decoding were adapted from Etter et al. (2020) and can be downloaded at the following address: https://github.com/etterguillaume/CaImDecoding. All other code is available from the corresponding authors upon request.

Statistics

Statistics Statistical analyses were performed using Matlab (Mathworks) and GraphPad Prism version 6.00 (GraphPad Software, La Jolla, California USA). All data are presented as mean ± standard error of the mean (SEM) and statistical test details are described in the corresponding results. All t-tests are two-tailed. Normality distribution of each group was assessed using the Shapiro-Wilk normality test and parametric tests were used only when distributions were found normal, using Student's t-tests, one-way ANOVA or two-way ANOVA. For non-normal distributions, non-parametric tests Mann-Whitney or Kruskal-Wallis tests were performed and described where applicable. Significant main effects or

interactions were followed up with appropriate post hoc testing using Bonferroni corrections were applicable. $p < 0.05$ was considered statistically significant, or $p < .01$ and described where applicable *, $p < 0.05$; **, $p < 0.01$; ***, $p < 0.001$, ****, $p < 0.0001$.

Funding

This work was supported by funding from the Canadian Institutes for Health Research (CIHR), Fonds de la Recherche en Santé du Québec (FRSQ), and the Natural Sciences and Engineering Research Council of Canada (NSERC). SVDV is supported by a Vanier Canada Graduate Scholarship and the Richard H. Tomlinson Doctoral Fellowship.

Acknowledgments

We thank Alexandra T. Keinath for very valuable comments on the manuscript. We thank Ke Cui for help with colony maintenance and mice perfusions, and members of the Williams lab for constructive feedback throughout the work. We also thank Daniel Aharoni (UCLA) for guidance in using the UCLA miniscope and Bruno Rivard for building the miniscopes. The present study used the services of the Molecular and Cellular Microscopy Platform at the DHRC.

Author contributions

SV and SW designed the study. SV performed surgeries, behavioral recording experiments, immunohistological experiments, and calcium data analysis. GE performed calcium data analysis and implanted mice for CA1 recordings. FS assisted with behavioral recording experiments, immunohistological experiments and performed quantifications. CAM implanted two mice that were used in the current study. SV and SW wrote the manuscript with inputs from all authors.

Competing interests

The authors declare no competing interests.

References

1. Paxinos, G. & Franklin, K. B. J. *The Mouse Brain in Stereotaxic Coordinates*. (Elsevier Academic Press, 2001).
2. Zhao, C., Eisinger, B. & Gammie, S. Characterization of GABAergic Neurons in the Mouse Lateral Septum: A Double Fluorescence In Situ Hybridization and Immunohistochemical Study Using Tyramide Signal Amplification. *PLoS One* **8**, 1–24 (2013).
3. Brito, G. N. O. & Thomas, G. J. T-maze alternation, response patterning, and septo-hippocampal circuitry in rats. *Behav. Brain Res.* **3**, 319–340 (1981).
4. Rawlins, J. N. P. & Olton, D. S. The septo-hippocampal system and cognitive mapping. *Behav. Brain Res.* **5**, 331–358 (1982).
5. Stanton, M. E., Thomas, G. J. & Brito, G. N. O. Posterodorsal septal lesions impair performance on both shift and stay working memory tasks. *Behav. Neurosci.* **98**, 405–415 (1984).
6. Thomas, G. J. Comparison of effects of small lesions in posterodorsal septum on spontaneous and rerun correction (contingently reinforced) alternation in rats. *J. Comp. Physiol. Psychol.* **93**, 685–694 (1979).
7. Thomas, G. J. & Brito, G. N. Recovery of delayed alternation in rats after lesions in medial frontal cortex and septum. *J. Comp. Physiol. Psychol.* **94**, 808–818 (1980).
8. Calderwood, M. T., Tseng, A. & Glenn Stanley, B. Lateral septum mu opioid receptors in stimulation of feeding. *Brain Res.* **1734**, 146648 (2020).

9. Carus-Cadavieco, M. *et al.* Gamma oscillations organize top-down signalling to hypothalamus and enable food seeking. *Nature* **542**, 232–236 (2017).

10. Sweeney, P. & Yang, Y. An Inhibitory Septum to Lateral Hypothalamus Circuit That Suppresses Feeding. *J. Neurosci.* **36**, 11185–11195 (2016).

11. Xu, Y. *et al.* Identification of a neurocircuit underlying regulation of feeding by stress-related emotional responses. *Nat. Commun.* **10**, (2019).

12. Anthony, T. E. *et al.* Control of stress-induced persistent anxiety by an extra-amygdala septohypothalamic circuit. *Cell* **156**, 522–536 (2014).

13. Besnard, A. *et al.* Dorsolateral septum somatostatin interneurons gate mobility to calibrate context-specific behavioral fear responses. *Nat. Neurosci.* (2019). doi:10.1038/s41593-018-0330-y

14. Sparks, P. & Ledoux, J. *The septal complex as seen through the context of fea, In: the behavioral neuroscience of the septal regino*. (Springer-Verlag, 2000).

15. Trent, N. L. & Menard, J. L. The ventral hippocampus and the lateral septum work in tandem to regulate rats' open-arm exploration in the elevated plus-maze. *Physiol. Behav.* **101**, 141–152 (2010).

16. Bender, F. *et al.* Theta oscillations regulate the speed of locomotion via a hippocampus to lateral septum pathway. *Nat. Commun.* **6**, 8521 (2015).

17. Wirtshafter, H. S. & Wilson, M. A. Locomotor and Hippocampal Processing Converge in the Lateral Septum Article Locomotor and Hippocampal Processing Converge in the Lateral Septum. *Curr. Biol.* **29**, 3177-3192.e3 (2019).

18. Bredewold, R., Schiavo, J. K., van der Hart, M., Verreij, M. & Veenema, A. H. Dynamic changes in extracellular release of GABA and glutamate in the lateral septum during social play behavior in juvenile rats: Implications for sex-specific regulation of social play behavior. *Neuroscience* **307**, 117–127 (2015).

19. Chee, S.-S. A., Menard, J. L. & Dringenberg, H. C. The lateral septum as a regulator of hippocampal theta oscillations and defensive behavior in rats. *J. Neurophysiol.* **113**, 1831–1841 (2015).

20. Clemens, A. M., Wang, H. & Brecht, M. The lateral septum mediates kinship behavior in the rat. *Nat. Commun.* **11**, 1–11 (2020).

21. Leroy, F. *et al.* A circuit from hippocampal CA2 to lateral septum disinhibits social aggression. *Nature* **564**, 213–218 (2018).

22. Risold, P. Y. & Swanson, L. W. Connections of the rat lateral septal complex. *Brain Res. Rev.* **24**, 115–195 (1997).

23. Swanson, L. W. & Cowan, W. M. An Autoradiographic Study of the Organization of the Efferent Connections of the Hippocampal Formation in the Rat. *J. Comp. Neur.* **172**, 49–84 (1977).

24. Tingley, D. & Buzsáki, G. Transformation of a Spatial Map across the Hippocampal-Lateral Septal Circuit. *Neuron* **98**, 1229-1242.e5 (2018).

25. Kita, T., Nishijo, H., Eifuku, S., Terasawa, K. & Ono, T. Place and contingency differential responses of monkey septal neurons during conditional place-object discrimination. *J. Neurosci.* **15**, 1683–1703 (1995).

26. Leutgeb, S. & Mizumori, S. Context-specific spatial representations by lateral septal cells. *Neuroscience* **112**, 655–663 (2002).

27. Nishijo, H., Kita, T., Tamura, R., Uwano, T. & Terasawa, K. Septal Neuronal Responses Related to Spatial Representation in Monkeys. *Hippocampus* **464**, 460–464 (1997).

28. Takamura, Y. *et al.* Spatial Firing Properties of Lateral Septal Neurons. **644**, 635–644 (2006).

29. Zhou, T. L., Tamura, R., Kuriwaki, J. & Ono, T. Comparison of Medial and Lateral

Septal Neuron Activity During Performance of Spatial Tasks in Rats. **234**, 220–234 (1999).

30. Wirtshafter, H. S. & Wilson, M. A. Differences in reward biased spatial representations in the lateral septum and hippocampus. *Elife* **9**, 1–20 (2020).

31. Monaco, J. D., De Guzman, R. M., Blair, H. T. & Zhang, K. *Spatial synchronization codes from coupled rate-phase neurons*. *PLoS Computational Biology* **15**, (2019).

32. Gonzalez, W. G., Zhang, H., Harutyunyan, A. & Lois, C. Persistence of neuronal representations through time and damage in the hippocampus. *Science (80-.).* **365**, 821–825 (2019).

33. Howard, M. W. & Kahana, M. J. A distributed representation of temporal context. *J. Math. Psychol.* **46**, 269–299 (2002).

34. Mankin, E. A., Diehl, G. W., Sparks, F. T., Leutgeb, S. & Leutgeb, J. K. Hippocampal CA2 Activity Patterns Change over Time to a Larger Extent than between Spatial Contexts. *Neuron* **85**, 190–202 (2015).

35. Rubin, A., Geva, N., Sheintuch, L. & Ziv, Y. Hippocampal ensemble dynamics timestamp events in long-term memory. *Elife* **4**, 1–16 (2015).

36. Ziv, Y. *et al.* Long-term dynamics of CA1 hippocampal place codes. *Nat. Neurosci.* **16**, 264–266 (2013).

37. Luo, A. H., Tahsili-Fahadan, P., Wise, R. A., Lupica, C. R. & Aston-Jones, G. Linking context with reward: A funcitonal circuit from hippocampal CA3 to Ventral Tegmental Area. *Science (80-.).* **333**, 353–357 (2011).

38. McGlinchey, E. M. & Aston-Jones, G. Dorsal hippocampus drives context-induced cocaine seeking via inputs to Lateral Septum. *Neuropsychopharmacology* **43**, 987–1000 (2018).

39. Butler, C. W., Wilson, Y. M., Gunnersen, J. M. & Murphy, M. Tracking the fear

memory engram: Discrete populations of neurons within amygdala, hypothalamus, and lateral septum are specifically activated by auditory fear conditioning. *Learn. Mem.* **22**, 370–384 (2015).

40. Garcia, R., Vouimba, R. M. & Jaffard, R. Contextual conditioned fear blocks the induction but not the maintenance of lateral septal LTP in behaving mice. *J. Neurophysiol*. **78**, 76–81 (1997).

41. Reis, D. G., Scopinho, A. A., Guimarães, F. S., Corrêa, F. & Resstel, L. B. M. Involvement of the lateral septal area in the expression of fear conditioning to context. *Learn. Mem.* **17**, 134–138 (2010).

42. Vetere, G. *et al*. Chemogenetic Interrogation of a Brain-wide Fear Memory Network in Mice. *Neuron* **94**, 363-374.e4 (2017).

43. Leutgeb, S. & Mizumori, S. Excitotoxic septal lesions result in spatial memory deficits and altered flexibility of hippocampal single-unit representations. *J. Neurosci*. **19**, 6661–72 (1999).

44. M'Harzi, M. & Jarrard, L. E. Effects of medial and lateral septal lesions on acquisition of a place and cue radial maze task. *Behav. Brain Res*. **49**, 159–165 (1992).

45. Zingg, B. *et al.* AAV-Mediated Anterograde Transsynaptic Tagging: Mapping Corticocollicular Input-Defined Neural Pathways for Defense Behaviors. *Neuron* **93**, 33–47 (2017).

46. Beier, K. T. *et al.* Circuit Architecture of VTA Dopamine Neurons Revealed by Systematic Input-Output Mapping Article Circuit Architecture of VTA Dopamine Neurons Revealed by Systematic Input-Output Mapping. *Cell* **162**, 622–634 (2015).

47. Etter, G., Manseau, F. & Williams, S. A Probabilistic Framework for Decoding Behavior From in vivo Calcium Imaging Data. *Front. Neural Circuits* **14**, 1–16 (2020).

48. Shannon, C. E. A mathematical theory of communication. *Bell Syst. Tech. J.* **27**, 379–

423 (1948).

49. Skaggs, W. E., McNaughton, B. L. & Gothard, K. M. An information-theoretic approach to deciphering the hippocampal code. in *Advances in Neural Information Processing Systems 5. eds. Hanson, S.J., Giles, C.L. & Cowan, J.D.* 1030–1037 (1993). doi:10.1109/EUMC.2007.4405137

50. Souza, B. C. ., Pavão, R., Belchior, H. & Tort, A. On Information Metrics for Spatial Coding. **375**, 62–73 (2018).

51. Pedemonte, M., Barrenechea, C., Nuñez, A., Gambini, J. P. & García-Austt, E. Membrane and circuit properties of lateral septum neurons: Relationships with hippocampal rhythms. *Brain Res.* **800**, 145–153 (1998).

52. Mau, W. *et al.* The Same Hippocampal CA1 Population Simultaneously Codes Temporal Information over Multiple Timescales. *Curr. Biol.* **28**, 1499-1508.e4 (2018).

53. Acharya, L., Aghajan, Z. M., Vuong, C., Moore, J. J. & Mehta, M. R. Causal Influence of Visual Cues on Hippocampal Directional Selectivity. *Cell* **164**, 197–207 (2016).

54. Leutgeb, S., Ragozzino, K. E. & Mizumori, S. Convergence of head direction and place information in the CA1 region of hippocampus. *Neuroscience* **100**, 11–19 (2000).

55. Muller, R. U., Bostock, E., Taube, J. S. & Kubie, J. On the directional firing properties of hippocampal place cells. *J. Neurosci.* **14**, 7235–7251 (1994).

56. Czurko, A., Hirase, H., Csicsvari, J. & Buzsáki, G. Sustained activation of hippocampal pyramidal cells by ‘space clamping’ in a running wheel. *Eur. J. Neurosci.* **11**, 344–352 (1999).

57. McNaughton, B. L., Barnes, C. A. & O’Keefe, J. The contributions of position, direction and velocity to single unit activity in the hippocampus of freely-moving rats. *Exp. Brain Res.* **52**, (1983).

58. Góis, Z. H. T. D. & Tort, A. B. L. Characterizing Speed Cells in the Rat Hippocampus. *Cell Rep*. **25**, 1872-1884.e4 (2018).

59. Markus, E. J. *et al*. Interactions between location and task affect the spatial and directional firing of hippocampal neurons. *J. Neurosci.* **15**, 7079–7094 (1995).

60. Navratilova, Z., Hoang, L. T., Daniela Schwindel, C., Tatsuno, M. & McNaughton, B. L. Experience-dependent firing rate remapping generates directional selectivity in hippocampal place cells. *Front. Neural Circuits* **6**, 1–14 (2012).

61. Raisman, G. The connexions of the septum. *Brain* **89**, 317–348 (1966).

62. Leranth, C., Deller, T. & Buzsáki, G. Intraseptal connections redefined: lack of a lateral septum to medial septum path. *Brain Res.* **583**, 1–11 (1992).

63. Staiger, J. F. & Nürnberger, F. The efferent connections of the lateral septal nucleus in the guinea pig: intrinsic connectivity of the septum and projections to other telencephalic areas. *Cell Tissue Res.* **264**, 415–426 (1991).

64. Swanson, L. W. & Cowan, W. M. The Connections of the Septal Region in the Rat. *J. Comp. Neur*. **186**, 621–656 (1979).

65. Witter, M. P., Daelmans, H. E., Jorritsma-Byham, B., Staiger, J. F. & Wouterlood, F. G. Restricted origin and distribution of projections from the lateral to the medial septal complex in rat and guinea pig. *Neurosci. Lett.* **148**, 164–168 (1992).

66. Patel, J., Schomburg, E. W., Bere, A. & Fujisawa, S. Local Generation and Propagation of Ripples along the Septotemporal Axis of the Hippocampus. **33**, 17029–17041 (2013).

67. Leão, R. N., Targino, Z. H., Colom, L. V. & Fisahn, A. Interconnection and synchronization of neuronal populations in the mouse medial septum/diagonal band of Broca. *J. Neurophysiol.* **113**, 971–980 (2015).

68. Robinson, J. *et al.* Optogenetic Activation of Septal Glutamatergic Neurons Drive

Hippocampal Theta Rhythms. **36**, 3016–3023 (2016).

69. Buzsáki, G. Theta oscillations in the hippocampus. *Neuron* **33**, 325–340 (2002).

70. Fuhrmann, F. *et al.* Locomotion, Theta Oscillations, and the Speed-Correlated Firing of Hippocampal Neurons Are Controlled by a Medial Septal Glutamatergic Circuit. *Neuron* **86**, 1253–1264 (2015).

71. Justus, D. *et al.* Glutamatergic synaptic integration of locomotion speed via septoentorhinal projections. *Nat. Neurosci.* **20**, 16–19 (2017).

72. Stuber, G. D. & Wise, R. A. Lateral Hypothalamic Circuits for Feeding and Reward. *Nat. Neurosci.* **19**, 198–205 (2016).

73. Burdakov, D. & Peleg-Raibstein, D. The hypothalamus as a primary coordinator of memory updating. *Physiol. Behav.* **223**, 112988 (2020).

74. Petrovich, G. D. Lateral hypothalamus as a motivation-cognition interface in the control of feeding behavior. *Front. Syst. Neurosci.* **12**, 1–7 (2018).

75. Kosse, C. & Burdakov, D. Natural hypothalamic circuit dynamics underlying object memorization Authors: *bioRxiv* (2019).

76. Izawa, S. *et al.* REM sleep-active MCH neurons are involved in forgetting hippocampusdependent memories. *Science (80-.).* **365**, 1308–1313 (2019).

77. Aitta-Aho, T., Pappa, E., Burdakov, D. & Apergis-Schoute, J. Cellular activation of hypothalamic hypocretin/orexin neurons facilitates short-term spatial memory in mice. *Neurobiol. Learn. Mem.* **136**, 183–188 (2016).

78. Sinnamon, H. M. Preoptic and hypothalamic neurons and the initiation of locomotion in the anesthetized rat. *Prog. Neurobiol.* **41**, 323–344 (1993).

79. Grillner, S., Wallén, P., Saitoh, K., Kozlov, A. & Robertson, B. Neural bases of goal-directed locomotion in vertebrates-An overview. *Brain Res. Rev.* **57**, 2–12 (2008).

80. Gladfelter, W. E. & Brobeck, J. R. Decreased spontaneous locomotor activity in the rat

induced by hypothalamic lesions. *Am. J. Physiol.* **203**, 811–817 (1962).

81. Kosse, C., Schöne, C., Bracey, E. & Burdakov, D. Orexin-driven GAD65 network of the lateral hypothalamus sets physical activity in mice. *Proc. Natl. Acad. Sci. U. S. A.* **114**, 4525–4530 (2017).

82. Mogenson, G. J., Jones, D. L. & Yim, C. Y. From motivation to action: Functional interface between the limbic system and the motor system. *Prog. Neurobiol.* **14**, 69–97 (1980).

83. Mahler, S. V., Moorman, D. E., Smith, R. J., James, M. H. & Aston-Jones, G. Motivational activation: A unifying hypothesis of orexin/hypocretin function. *Nat. Neurosci.* **17**, 1298–1303 (2014).

84. Buzsáki, G. & Tingley, D. Space and Time: The Hippocampus as a Sequence Generator. *Trends Cogn. Sci.* (2018). doi:10.1016/j.tics.2018.07.006

85. Danielson, N. B. *et al.* Sublayer-Specific Coding Dynamics during Spatial Navigation and Learning in Hippocampal Area CA1. *Neuron* **91**, 652–665 (2016).

86. Masurkar, A. V. *et al.* Medial and lateral entorhinal cortex differentially excite deep versus superficial CA1 pyramidal neurons. *Cell Rep.* **18**, 139–148 (2017).

87. Gauthier, J. L. & Tank, D. A Dedicated Population for Reward Coding in the Article A Dedicated Population for Reward Coding in the Hippocampus. *Neuron* **99**, 179-193.e7 (2018).

88. Taube, J., Muller, R. & Ranck, J. Head-direction cells recorded from the postsubiculum in freely moving rats. I. Description and quantitative analysis. *J. Neurosci.* **10**, 420–435 (1990).

89. Taube, J. S. Head direction cells recorded in the anterior thalamic nuclei of freely moving rats. *J. Neurosci.* **15**, 70–86 (1995).

90. Stackman, R. W. & Taube, J. S. Firing properties of rat lateral mammillary single

units: Head direction, head pitch, and angular head velocity. *J. Neurosci.* **18**, 9020–9037 (1998).

91. Sargolini, F. *et al.* Conjunctive representation of position, direction, and velocity in entorhinal cortex. *Science (80-.).* **312**, 758–762 (2006).

92. Oh, S. W. *et al.* A mesoscale connectome of the mouse brain. *Nature* **508**, 207–214 (2014).

93. Luo, A. H., Tahsili-fahadan, P., Wise, R. A., Lupica, C. R. & Aston-jones, G. Supporting Online Material for CA3 to Ventral Tegmental Area. (2011). doi:10.1126/science.1204622

94. Pastalkova, E., Itskov, V., Amarasingham, A. & Buzsáki, G. Internally generated cell assembly sequences in the rat hippocampus. *Science (80-.).* **321**, 1322–1328 (2008).

95. Eichenbaum, H. Time cells in the hippocampus: A new dimension for mapping memories. *Nat. Rev. Neurosci.* **15**, 732–744 (2014).

96. Deshmukh, S. S. & Bhalla, U. S. Representation of odor habituation and timing in the hippocampus. *J. Neurosci.* **23**, 1903–1915 (2003).

97. MacDonald, C. J., Carrow, S., Place, R. & Eichenbaum, H. Distinct hippocampal time cell sequences represent odor memories in immobilized rats. *J. Neurosci.* **33**, 14607–14616 (2013).

98. Aronov, D., Nevers, R. & Tank, D. W. Mapping of a non-spatial dimension by the hippocampal-entorhinal circuit. *Nature* **543**, 719–722 (2017).

99. Pnevmatikakis, E. A. & Giovannucci, A. NoRMCorre: An online algorithm for piecewise rigid motion correction of calcium imaging data. *J. Neurosci. Methods* **291**, 83–94 (2017).

100. Zhou, P. *et al.* Efficient and accurate extraction of in vivo calcium signals from microendoscopic video data. (2017). doi:http://arxiv.org/abs/1605.07266

101. Cohen, M. X. *Analyzing Neural Time Series Data: Theory And Practice.* (The MIT Press, 2014).

102. Sheintuch, L. *et al.* Tracking the Same Neurons across Multiple Days in Ca2+Imaging Data. *Cell Rep.* **21**, 1102–1115 (2017).

Main Figures

Figure 1: LS receives inputs from the hippocampal subregions. a, Strategy for retrograde rabies tracing in LS. b, Injection site, blue = DAPI staining, green = TVA.oG coupled to an enhanced green fluorescent protein (eGFP), red = Rabies coupled to mCherry, orange: starter cells expressing both TVA.oG.eGFP and Rabies.mCherry. c, Retrograde transfection in the dorsal hippocampus, coronal section. Bottom left: example of transfected CA1 pyramidal cell, bottom right: transfected CA3 pyramidal cells. d, Coronal section of ventral hippocampal region, showing retrograde transfected cell bodies at the level of both subiculum, CA1 and CA3. e, Transfected cell bodies at the fasciola cinereum (FC). f, Mean number of cells found at the level of the hippocampus for each 300μm coronal section. g, Retrogradely transfected cells in the ventral tegmental area (VTA). h, Bilateral transfection of the hypothalamic region. i, Cell bodies in the PAG. Scale bars: b, top: 300 μm, bottom left, middle, and right: 50 μm. c, top: 500 μm, bottom left and right 50 μm, d, left: 500 μm, right: 300 μm. e, 200 μm. g, 500 μm, h, 500 μm and i, 400 μm. *, $p < .05$, **, $p < .01$, ***, $p <$

.001, ns = not significant. Test used in g, one-way ANOVA. Sub = subiculum, FC = fasciola cinereum, Aq = aqueduct, mtg = mammillotegmental tract, VTA = ventral tegmental area, MM = medial mammilary nucleus, PH = posterior hypothalamic area, 3V = third ventricle, LH = lateral hypothalamus, f = fornix, PAG = periaqueductal grey.

Figure 2: Anterograde transsynaptic tracing shows that CA1 and CA3 project preferentially to dorsal LS, which projects in turn to LH and MS. a, Diagram of dual-viral injection strategy for anterograde transsynaptic tracing. The diagram is based on dorsal CA1 targeted injection, dCA3 is also used for injections. b, Coronal section showing primary injection site in dorsal CA1 (top) or dorsal CA3 (bottom). Red = tdTom expression, blue = DAPI, with zoomed images showing transfected cell bodies are predominantly located in the pyramidal layer (bottom). c, Coronal section showing transfection pattern at different anterior-posterior levels of the LS, with (red) tdTOM positive CA3 projections to LS and eYFP-positive second-order transfection in LS (left). Bottom schematic: an overview of the approximate bregma level of coronal slices shown. Bottom right: Zoomed versions showing tdTom-positive hippocampal afferents, eYFP-positive transfected LS cell bodies, and merge. d, Total transfected cells counted at the level of LS following transsynaptic tracer injection in dCA1 versus dCA3 (dCA1-LS, N = 3 mice; dCA3-LS, N = 5 mice). e, Total transfected cells along the dorsal-ventral and anterior-posterior axis observed in LS for dorsal CA3 injection and f, for dorsal CA1 injection. g, eYFP-positive cell bodies at the anterior dorsal LS and fibers at the level of the medial septum following dCA1 injection (left) and dCA3 injection (right). Inset left: eYFP-positive fibers at the level of MS. h, Second-order transfection is seen bilaterally at the level of the lateral hypothalamus following dCA1 injection (left) and dCA3 injection (right). i, Injection strategy for Cre-dependent AAV. Synaptag mediated tracing in the LS. j, Coronal section of transfection at the level of dorsal LS, with

synaptophysin-bound eYFP at the MS. Top right: Zoomed images showing transfection at the injection site. Bottom right: eYFP-positive fibers. k, Schematic with proposed connections of the LS within the hippocampal network. Scale bars: b, top: 500 μm, bottom: 500 μm. c, all overview images, 500 μm, all zoomed images, 50 μm. g, left and right: 800 μm. h, left and right: 500 μm, bottom: 200 μm. j, left: 500 μm, top right: 100 μm, bottom right: 100 μm. ns = not significant. Test used in d, Mann Whitney test. DM = dorsomedial hypothalamic nucleus, 3V = third ventricle, LH = lateral hypothalamus. See also Supplemental Fig. 1.

Figure 3: GABAergic cells in the lateral septum are significantly spatially modulated during free exploration in an open field. a, Diagram of one-photon calcium recording setup in the lateral septum (bottom left) in freely behaving mice exploring an open field (top left), extracted spatial footprints (top right), and histological verification of implantation site (bottom right). b, Example of raw calcium fluorescence trace (top), and binarized events color-coded for time spent in the open field (bottom). Trace is divided into early and late recording epochs using 50% of total calcium (using the area under the curve). Inset: zoomed calcium trace with binarized traces. c, Open field with trajectory (gray) with corresponding activity (colored dots), activity is color-coded from start to end of the recording similar to b. d, Probability P (active | location) of an example cell to be active in a bin (3 cm) of the open field (45 or 49 cm size). e, Significance computed from n = 1000 circular permutations, $p < .01$ is considered significant. f, Within session stability is computed by correlation of first half (left) and the second half (right) of the recording. g, Method for computing the MI and 95% confidence interval from bootstrapped samples (left) and 30x shuffled surrogates (right). h, MI computed from actual traces (black) and shuffled traces (red), sorted by the magnitude of the difference between these values. Left inset: zoomed version of j for the first 20 cells. Right inset: zoomed version of j for 20 not significant cells. i, Examples of spatially

modulated (top) and non-spatially modulated cells using this metric, see also Supplemental Fig. 3. j, Proportion of LS neurons significantly spatially modulated for the overall population (N = 28 mice, n = 1899 cells). k, Percentage of spatially modulated cell per animal (N = 28). l, computation of activity index (probability inactive to active) and bursting index (probability active to active). m, Left: Activity index for spatial vs. non-spatial cells. Right: Bursting index for spatial versus non-spatial cells. n, Method for computing mean decoding accuracy using 30 bootstrapped samples, trained on 50% of the recorded data. o, Method for computing the Euclidean distance mean decoding error in cm for each bootstrapped estimate for open field recordings. p, Method for computing the mean decoding agreement for each bootstrapped estimate for open field recordings. q, Decoding error for actual vs shuffled dataset (30 times bootstrapped sample of n = 100 cells, N = 6 mice, see also Supplemental Fig. 5a. r, Decoding agreement (bootstrapped sample of n = 100 cells, N = 6 mice), see also Supplemental Fig. 5a. s, Strategy to record from different anterior-posterior levels in LS (left) and example of the range of implantation sites covered (for all animals, see Supplemental Fig. 6 and Supplemental Fig. 7. t, Strategy to approximate cell location. Background: Maximal projection of representative recording, red: outline of approximated GRIN lens position, white: distance from the center of the GRIN lens to the cells of interest. u, Probability being active for all spatial cells recorded along the anterior-posterior axis (left) and dorsal-ventral axis (right), x-axis = distance from bregma (mm). v, Proportion of stable (within-session stability > .5) place cells for .2 mm bins. Each dot represents the average per animal per bin along the anterior-posterior axis (left) and along the dorsal-ventral axis (right, N = 24 mice). Black lines indicate 95% confidence interval. Scale bar: a, 500 μm. **, $p < .01$, ****, $p < .0001$. Test used in h, two-way ANOVA, Sidak's multiple comparisons post hoc test. m, Mann-Whitney test, q-r, paired t-test, u, linear regression

Figure 4: LS GABAergic cells encode head direction, speed, and acceleration. a, Activity of an example LS neuron during free exploration in an open field, top: head direction (HD, red), middle: binarized activity (yellow), bottom: raw calcium activity (blue). b, Polar plot indicating the probability of the cell being active as a function of the animals' HD with (black, p(active | bin), red lines indicate 95% upper and lower percentile. MI calculated using 15° bins. c, Histogram showing the frequency of occurrence of the MI for recorded LS population (n = 1442 cells, N = 21 mice), see also Supplemental Fig. 8. d, Proportion of significantly directionally modulated cells using metrics described in Fig. 3 (bootstrapped MI significantly different from circularly shuffled, 30 bootstrapped samples, 50% sampling). e, Activity of an example LS neuron during free exploration modulated by velocity (top, red), middle: binarized activity (yellow), bottom: raw calcium activity (blue). f, Tuning curve for velocity for the example cell (red) with 95% upper and lower percentile in grey. MI calculated using 20 bins. g, Histogram showing the frequency of occurrence of the MI for recorded LS population (n = 1899 cells, N = 28 mice). h, Proportion of significantly velocity modulated cells. i, Activity of an example LS neuron during free exploration modulated by acceleration (top, red), middle: binarized activity (yellow), bottom: raw calcium activity (blue). j, Same as f, for acceleration. k, Same as g, for acceleration. l, Same as h, for acceleration. m, Example of an LS cell that is both significantly head direction modulated (left), as well as spatially modulated (right). n, Proportion of cells that are significantly modulated by only one modality (grey), two modalities (yellow), three (red) or all 4 of the investigated variables (black). The number above the bars indicates the absolute number of cells found to be modulated in the total population (n = 1230 cells, N = 19 mice). o, Absolute proportion of cells modulated by any combination of variables. p, Left: Proportion of directionally modulated cells for .2 mm bins. Each dot represents the average per animal per bin along dorsal-ventral axis (top), and along anterior-posterior axis (bottom, N = 17 mice),

Middle: same as left, but for velocity modulated cells (N = 24 mice). Bottom: same as left, but for acceleration modulated cells (N = 24 mice). Black lines indicate 95% confidence interval. q, Method for computing the mean decoding agreement for each bootstrapped estimate for head direction. r, Decoding error for actual vs shuffled dataset (30 times bootstrapped sample of n = 100 cells, N = 4 mice) and decoding agreement (bootstrapped sample of n = 100 cells, N = 4 mice). *, $p < .05$, **, $p < .01$, ***, $p < .001$. Test used in d, Mann Whitney test, g-h, paired t-test, k, Kruskall Wallis, Dunn's multiple comparisons, o, one-way ANOVA. HD = head direction, A = acceleration, S = spatial coding, V = velocity.

Figure 5: LS has an equal number of spatially modulated cells as the hippocampus, but its place fields are less stable and more dispersed. a, Top: Diagram of one-photon calcium recording setup in CA1 and CA3 in freely behaving mice exploring an open field (top left), middle: histological verification of implantation site and extracted calcium transients for LS, CA1 and CA3. b, Tuning curves of example place cells recorded in a 45 cm open field (3 cm bins). c, Proportion of place cells per animal (LS: n = 1899 cells from N = 28 mice; dCA1: n = 1229 cells, N = 6 mice; dCA3: n = 204 cells, N = 4 mice). d, Within session stability for spatial cells (LS: n = 734 place cells from N = 28 mice; dCA1: n = 424 place cells, N = 6 mice; dCA3: n = 86 place cells, N = 4 mice). e, Probability of being active for spatial cells (LS: n = 734 place cells from N = 28 mice; dCA1: n = 424 place cells, N = 6 mice; dCA3: n = 86 place cells, N = 4 mice). f, Left: mean dispersion computation, right: mean dispersion for spatial cells (LS: n = 734 place cells from N = 28 mice; dCA1: n = 424 place cells, N = 6 mice; dCA3: n = 86 place cells, N = 4 mice). g, Left: method for computing the mean decoding agreement for each bootstrapped estimate using 80 cells, (middle) decoding agreement and (right) decoding error for LS versus CA1 and CA3. 30 times bootstrapped sample of n = 90 cells, LS: N = 9 mice, CA1: N = 3 mice, CA3: N = 2 mice. *, $p < .05$, **, p

< .01, ***, p < .001, ****, p < .0001. Test used in c, one way ANOVA, d-g, Kruskall Wallis, Dunn's multiple comparisons.

Figure 6: Lateral septum cells are spatially tuned on a linear track alternation task. a, Recording strategy in the LS (left), with animal alternating left and right trajectories to obtain a sucrose reward on a 100 cm linear track. b, Probability of an example cell to be active given the location on the linear track (red) with 95% upper and lower percentile (grey) and the corresponding MI (top). Examples shown are from two different mice. c, Proportion of spatially modulated cells using metrics described above (n = 1030 cells from N = 15 mice). d, Left: Group averages of actual (grey) versus shuffled (red) MI for spatially modulated LS cells recorded on linear track. Right: group averages of spatial cells (grey) versus non-spatial cells (red) for split half stability. e, Top: Posterior probabilities for each frame estimated from binarized calcium activity, bottom: corresponding actual (green) and decoded (red) location. f, Method for computing the Euclidean distance mean decoding error in cm for each bootstrapped estimate and mean decoding agreement for each bootstrapped estimate for open field recordings. g, Decoding error for actual vs shuffled dataset (30 times bootstrapped sample of 100 cells, N = 4 mice). h, Decoding agreement for actual vs shuffled dataset (bootstrapped sample of n = 100 cells, N = 4 mice). i, Sorted place fields for a representative LS, CA1 and CA3 recording. j, Proportion of significantly spatially modulated cells for each recording region (CA1: n = 1148 cells, N = 5 mice, CA3: n = 144 cells, N = 2 mice). k, Left: split half stability of recorded spatial cells in each region and right: probability being active (LS: n = 475 cells, CA1: n = 336 cells, CA3: n = 47 cells). l, Mouse location on linear track, divided in left runs (orange) and right runs (light blue) with corresponding raw calcium activity (middle, dark blue) and derived binary trace (bottom, yellow). m, Probability of cell being active for left (orange) versus right trajectories (blue), and corresponding mutual

information calculated separately for left and right runs. n, Corresponding locations where binarized activity was detected (orange for left trajectories, blue for right trajectories and black for all trajectories). o, MI values for right versus left trajectories ranked by magnitude of the difference between the two. Dotted line $p < .01$ significance level. p, Proportion of spatially modulated cells in LS that are right-selective (blue, 22.08%), left-selective (orange, 15.52%), spatially modulated but not directionally modulated (red, 7.67%) and non-spatially modulated (grey, 54,71%, left), CA1 (middle) and CA3 (right). *, $p < .05$, ****, $p < .0001$, Test used in d, Mann-Whitney test, g, paired t-tests, k, Kruskal-Wallis, Dunn's multiple comparisons test, o, two-way ANOVA, Sidak's multiple comparisons post hoc test.

Figure 7: LS place code is similar to CA1 over longer periods of time. a, Experimental setup (top) and spatial footprints of cells recorded over days (bottom). b, Tuning maps for two sets of stable cells recorded over all days, with each row being one aligned cell. Tuning map correlation indicated at the bottom. c, Tuning map correlation for all aligned place cells (black) versus shuffled cells (red) for progressive days (day 1-2: n = 33 cells; day 2-3: n = 33 cells, day 3-8: n = 51 cells, N = 3 mice). d, Tuning map correlation for all aligned cells (black) versus shuffled cells (red) for progressive days. e, Proportion of place cells recorded for each day. Each dot is an animal (N = 5). f, Within session stability for each place cell for all recorded cells (day 1, n = 181; day 2, n = 172; day 3, n = 178; day 8, n = 209, N = 5 mice). g, Average MI for each day for all recorded cells (day 1, n = 562; day 2, n = 600; day 3, n = 477; day 8, n = 492, n = 5 mice). h, Probability being active for each recorded cell on eah day (day 1, n = 562; day 2, n = 600; day 3, n = 477; day 8, n = 492, n = 5 mice). i, Matrix of mean tuning map correlation for all aligned place cells recorded in LS (N = 3 mice) and CA1 (N = 1 mouse). j, Tuning map correlation between day 1 and day 8 for all aligned place cells recorded in LS vs CA1 (LS: 42 cells, n = 3 mice, CA1: 28 cells, n = 1 mouse). *, $p < .05$, **,

$p < .01$, ****, $p < .0001$. Test used in d, one-way ANOVA, e, two-way ANOVA, Sidak's multiple comparisons test, f, Kruskall Wallis test, with Dunn's multiple comparison test. g-h, Kruskall Wallis test, j, unpaired t-test.

Figure 1

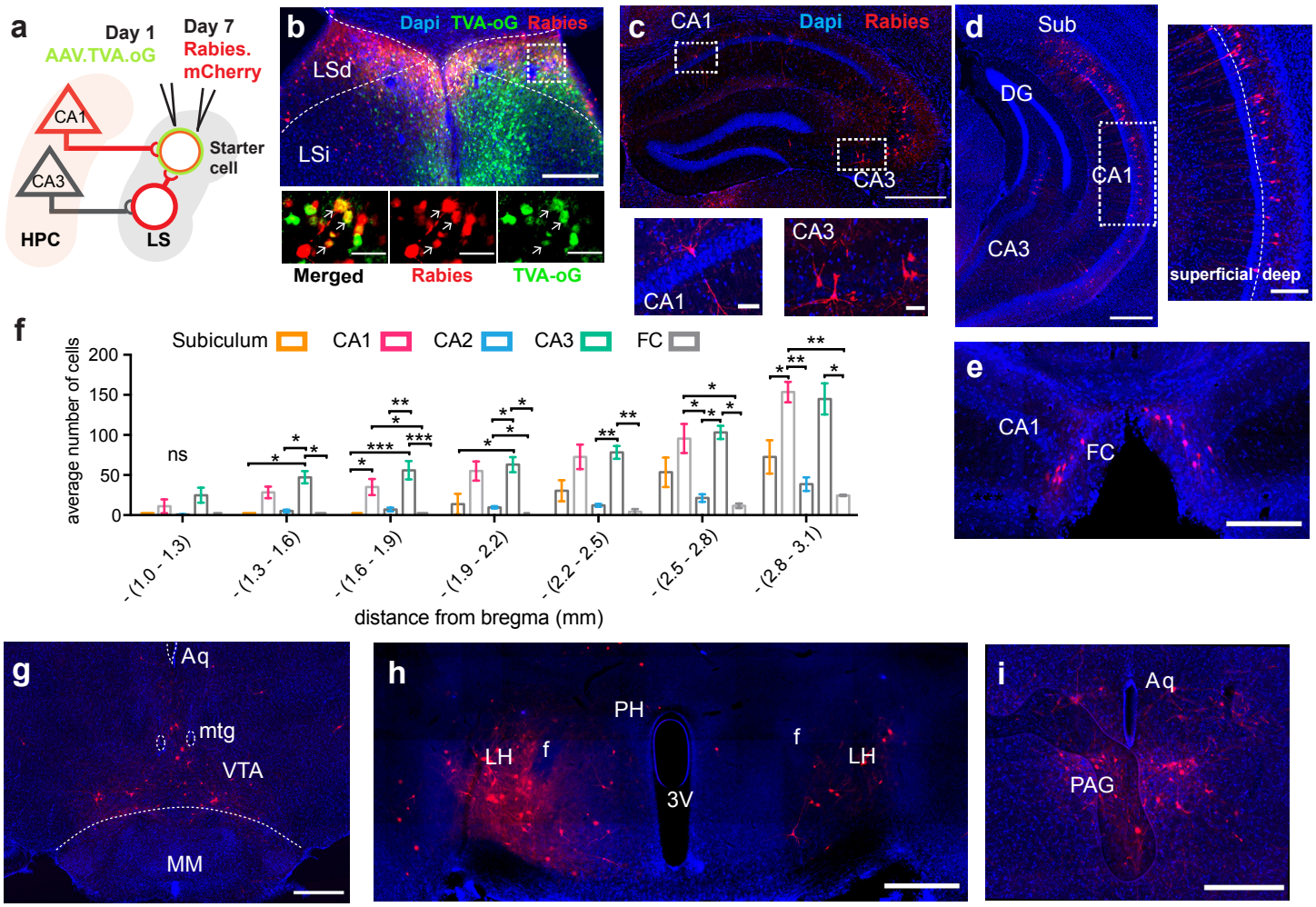
a
Day 1
AAV.TVA.oG
Day 7
Rabies.
mCherry
CA1
CA3
Starter cell
HPC
LS
b
Dapi TVA-oG Rabies
LSd
LSi
Merged
Rabies
TVA-oG
c
CA1
Dapi Rabies
CA3
CA1
CA3
d
Sub
DG
CA1
CA3
superficial deep
e
CA1
FC
f
Subiculum CA1 CA2 CA3 FC
average number of cells
200
150
100
50
0
ns
- (1.0 - 1.3)
- (1.3 - 1.6)
- (1.6 - 1.9)
- (1.9 - 2.2)
- (2.2 - 2.5)
- (2.5 - 2.8)
- (2.8 - 3.1)
distance from bregma (mm)
g
Aq
mtg
VTA
MM
h
PH
LH
f
3V
f
LH
i
Aq
PAG

Figure 2

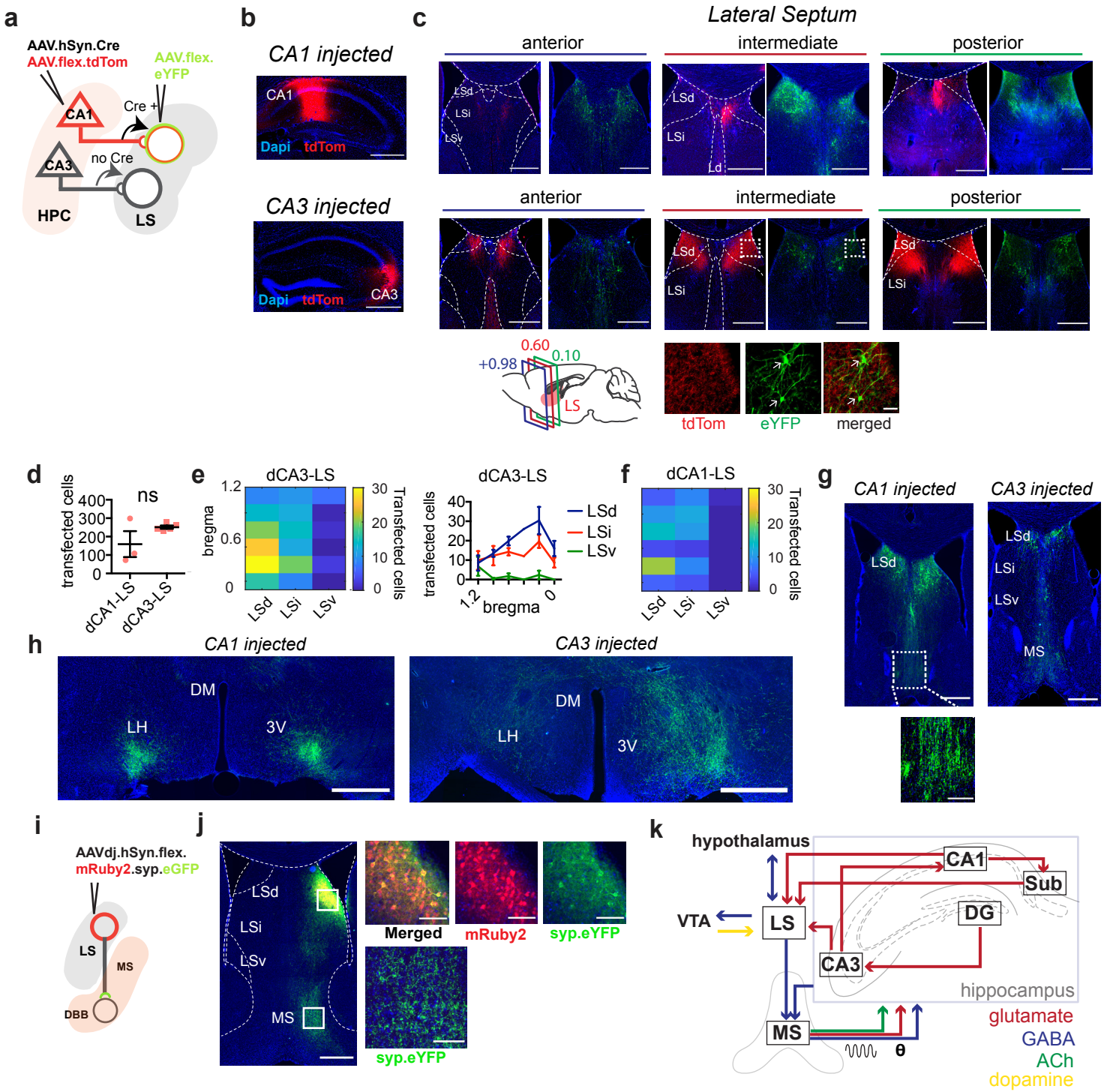
a
AAV.hSyn.Cre
AAV.flex.tdTom
AAV.flex.
eYFP
CA1
Cre +
CA3
no Cre
HPC
LS
b
CA1 injected
CA1
Dapi tdTom
CA3 injected
Dapi tdTom
CA3
c
Lateral Septum
anterior
intermediate
posterior
LSd
LSi
LSv
Ld
0.60
0.10
+0.98
LS
tdTom
eYFP
merged
d
transfected cells
ns
dCA1-LS
dCA3-LS
e
dCA3-LS
bregma
Transfected cells
LSd
LSi
LSv
f
dCA1-LS
g
CA1 injected
CA3 injected
h
CA1 injected
CA3 injected
DM
LH
3V
MS
i
AAVdj.hSyn.flex.
mRuby2.syp.eGFP
LS
MS
DBB
j
Merged
mRuby2
syp.eYFP
k
hypothalamus
VTA
LS
CA1
Sub
DG
CA3
hippocampus
MS
θ
glutamate
GABA
ACh
dopamine

Figure 3

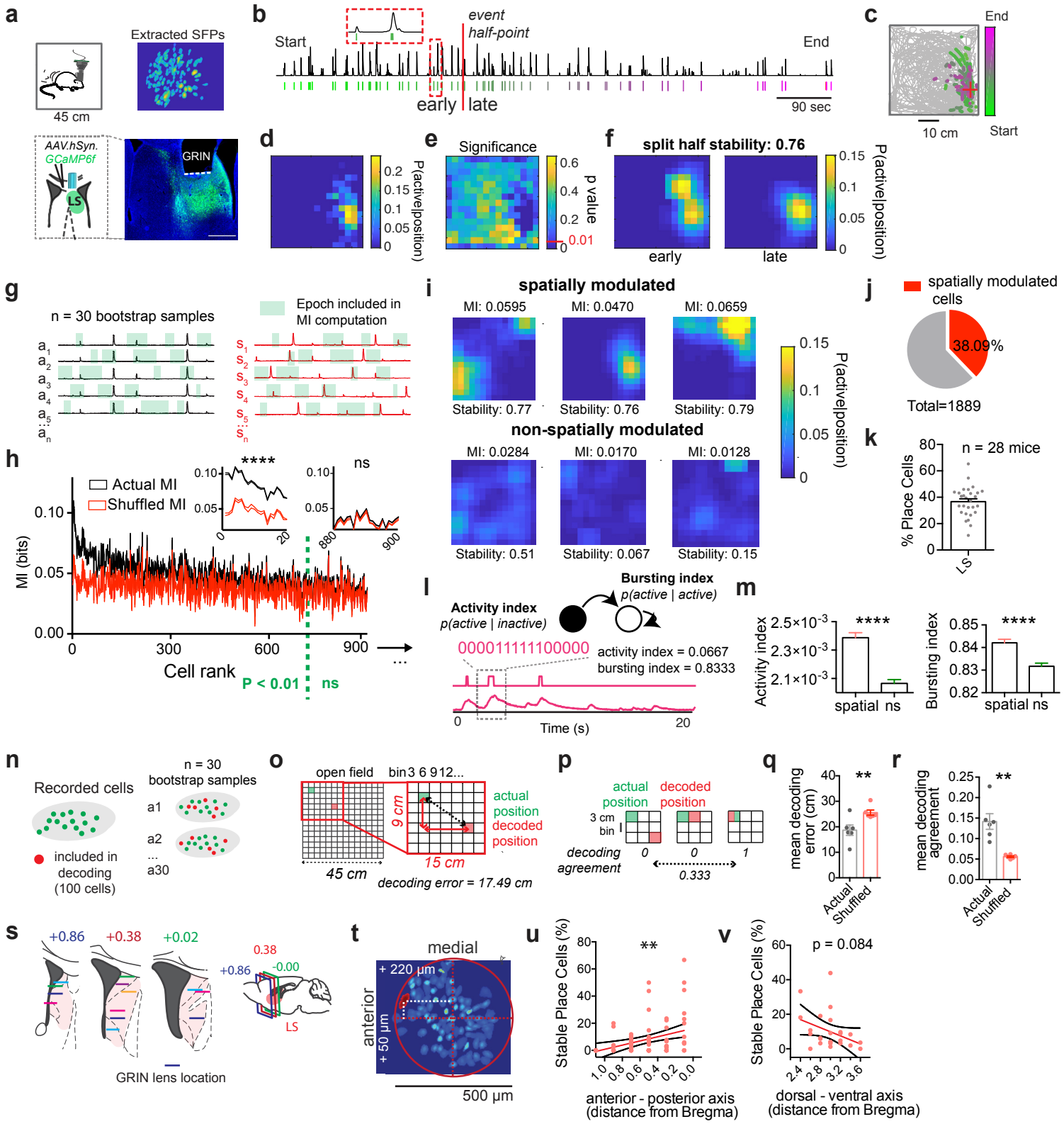
a
Extracted SFPs
45 cm
AAV.hSyn.
GCaMP6f
LS
GRIN
b
Start
event
half-point
End
early
late
90 sec
c
End
10 cm
Start
d
P(active|position)
e
Significance
p value
0.01
f
split half stability: 0.76
early
late
P(active|position)
g
n = 30 bootstrap samples
Epoch included in MI computation
h
Actual MI
Shuffled MI
MI (bits)
Cell rank
P < 0.01
ns
****
ns
i
spatially modulated
MI: 0.0595
MI: 0.0470
MI: 0.0659
Stability: 0.77
Stability: 0.76
Stability: 0.79
non-spatially modulated
MI: 0.0284
MI: 0.0170
MI: 0.0128
Stability: 0.51
Stability: 0.067
Stability: 0.15
P(active|position)
j
spatially modulated cells
38.09%
Total=1889
k
n = 28 mice
% Place Cells
LS
l
Activity index
p(active | inactive)
Bursting index
p(active | active)
00001111100000
activity index = 0.0667
bursting index = 0.8333
Time (s)
m
Activity index
****
spatial
ns
Bursting index
****
spatial
ns
n
Recorded cells
n = 30
bootstrap samples
a1
a2
a30
included in decoding (100 cells)
o
open field
bin 3 6 9 12...
9 cm
15 cm
45 cm
actual position
decoded position
decoding error = 17.49 cm
p
actual position
decoded position
3 cm bin
decoding agreement
0.333
q
mean decoding error (cm)
**
Actual
Shuffled
r
mean decoding agreement
**
Actual
Shuffled
s
+0.86
+0.38
+0.02
0.38
+0.86
-0.00
LS
GRIN lens location
t
medial
anterior
+ 220 µm
+ 50 µm
500 µm
u
Stable Place Cells (%)
**
anterior - posterior axis
(distance from Bregma)
v
Stable Place Cells (%)
p = 0.084
dorsal - ventral axis
(distance from Bregma)

Figure 4

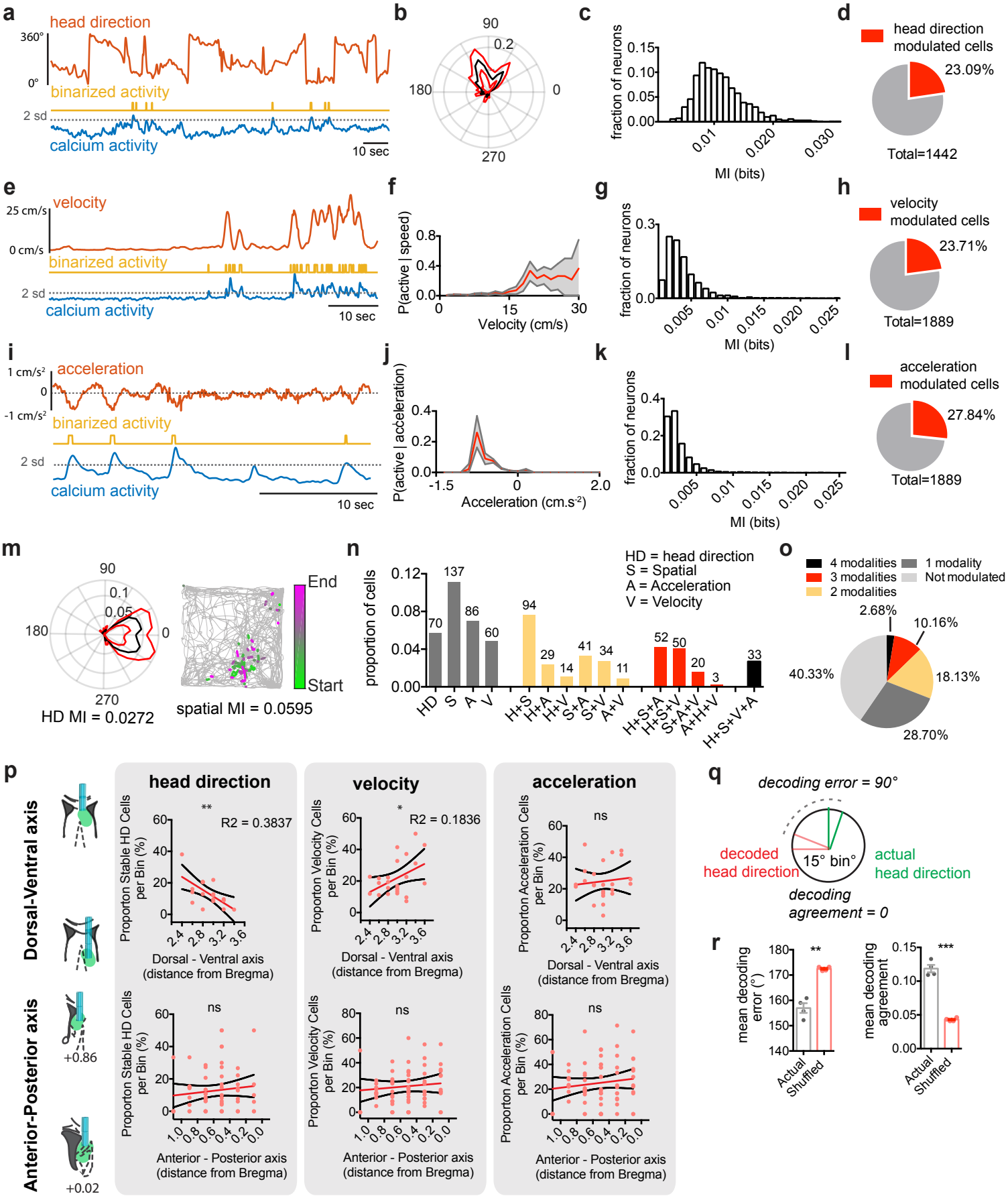
a
head direction
360°
0°
binarized activity
2 sd
calcium activity
10 sec
b
90
0.2
180
0
270
c
fraction of neurons
0.15
0.10
0.05
0.00
0.01
0.020
0.030
MI (bits)
d
head direction modulated cells
23.09%
Total=1442
e
velocity
25 cm/s
0 cm/s
binarized activity
2 sd
calcium activity
10 sec
f
P(active | speed)
0.8
0.4
0.0
0
15
30
Velocity (cm/s)
g
fraction of neurons
0.3
0.0
0.005
0.01
0.015
0.020
0.025
MI (bits)
h
velocity modulated cells
23.71%
Total=1889
i
acceleration
1 cm/s²
0
-1 cm/s²
binarized activity
2 sd
calcium activity
10 sec
j
P(active | acceleration)
0.4
0.2
0.0
-1.5
0
2.0
Acceleration (cm.s⁻²)
k
fraction of neurons
0.4
0.2
0.0
0.005
0.01
0.015
0.020
0.025
MI (bits)
l
acceleration modulated cells
27.84%
Total=1889
m
90
0.1
0.05
180
0
270
HD MI = 0.0272
End
Start
spatial MI = 0.0595
n
proportion of cells
0.12
0.08
0.04
0.00
HD = head direction
S = Spatial
A = Acceleration
V = Velocity
70
137
86
60
94
29
14
41
34
11
52
50
20
3
33
HD
S
A
V
H+S
H+A
H+V
S+A
S+V
A+V
H+S+A
H+S+V
S+A+V
A+H+V
H+S+V+A
o
4 modalities
3 modalities
2 modalities
1 modality
Not modulated
2.68%
10.16%
40.33%
18.13%
28.70%
p
Dorsal-Ventral axis
Anterior-Posterior axis
+0.86
+0.02
head direction
velocity
acceleration
Proporton Stable HD Cells per Bin (%)
Proporton Velocity Cells per Bin (%)
Proporton Acceleration Cells per Bin (%)
**
R2 = 0.3837
*
R2 = 0.1836
ns
Dorsal - Ventral axis (distance from Bregma)
Anterior - Posterior axis (distance from Bregma)
q
decoding error = 90°
decoded head direction
15° bin°
actual head direction
decoding agreement = 0
r
mean decoding error (°)
mean decoding agreement
**
***
Actual
Shuffled

Figure 5

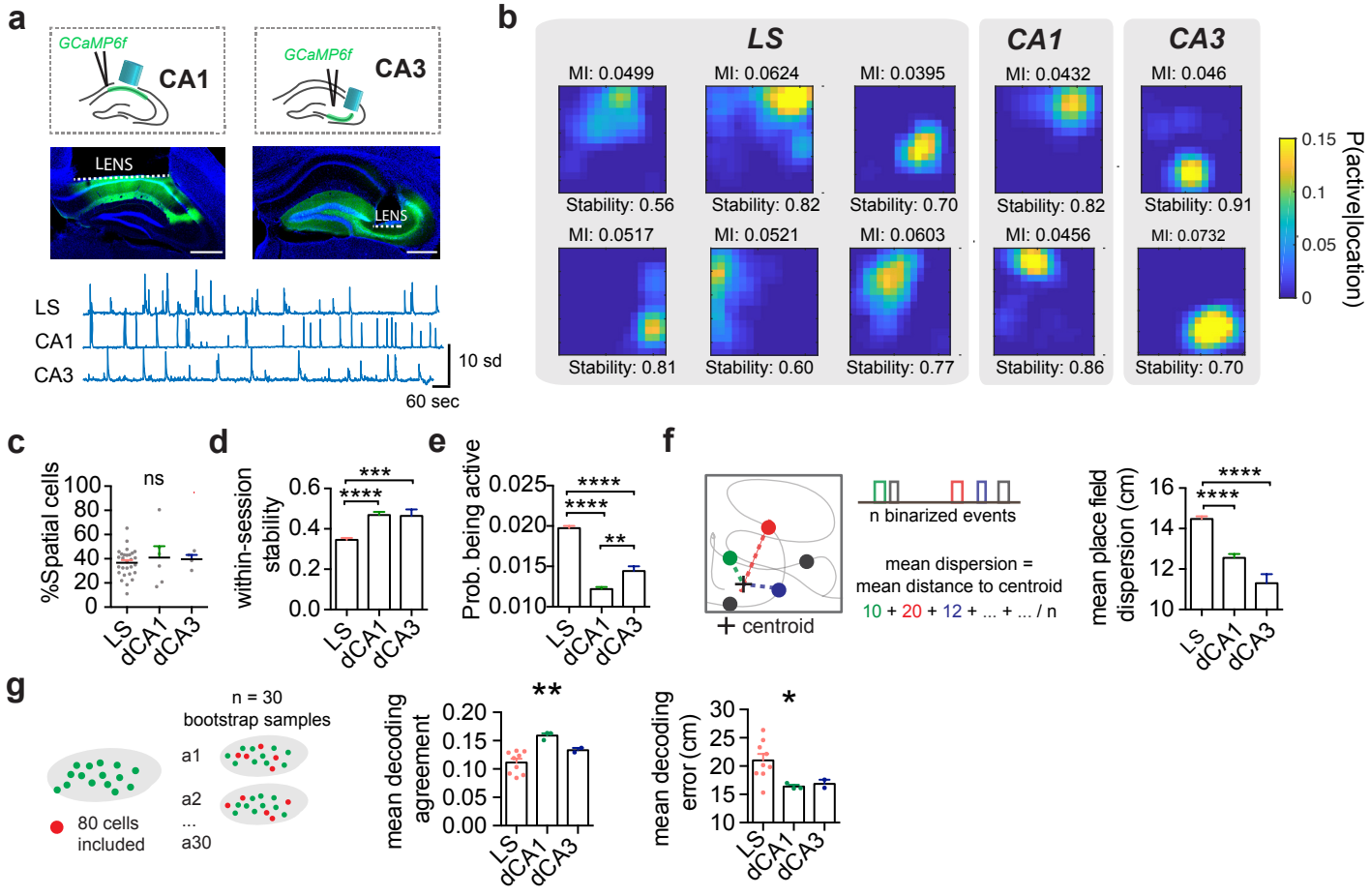
a
GCaMP6f
CA1
GCaMP6f
CA3
LENS
LENS
LS
CA1
CA3
10 sd
60 sec
b
LS
CA1
CA3
MI: 0.0499
MI: 0.0624
MI: 0.0395
MI: 0.0432
MI: 0.046
Stability: 0.56
Stability: 0.82
Stability: 0.70
Stability: 0.82
Stability: 0.91
MI: 0.0517
MI: 0.0521
MI: 0.0603
MI: 0.0456
MI: 0.0732
Stability: 0.81
Stability: 0.60
Stability: 0.77
Stability: 0.86
Stability: 0.70
P(active|location)
0.15
0.1
0.05
0
c
%Spatial cells
ns
LS
dCA1
dCA3
d
within-session stability
***
****
e
Prob. being active
****
****
**
f
+ centroid
n binarized events
mean dispersion =
mean distance to centroid
10 + 20 + 12 + ... + ... / n
mean place field dispersion (cm)
****
****
g
n = 30
bootstrap samples
a1
a2
...
a30
80 cells included
mean decoding agreement
**
mean decoding error (cm)
*

Figure 6

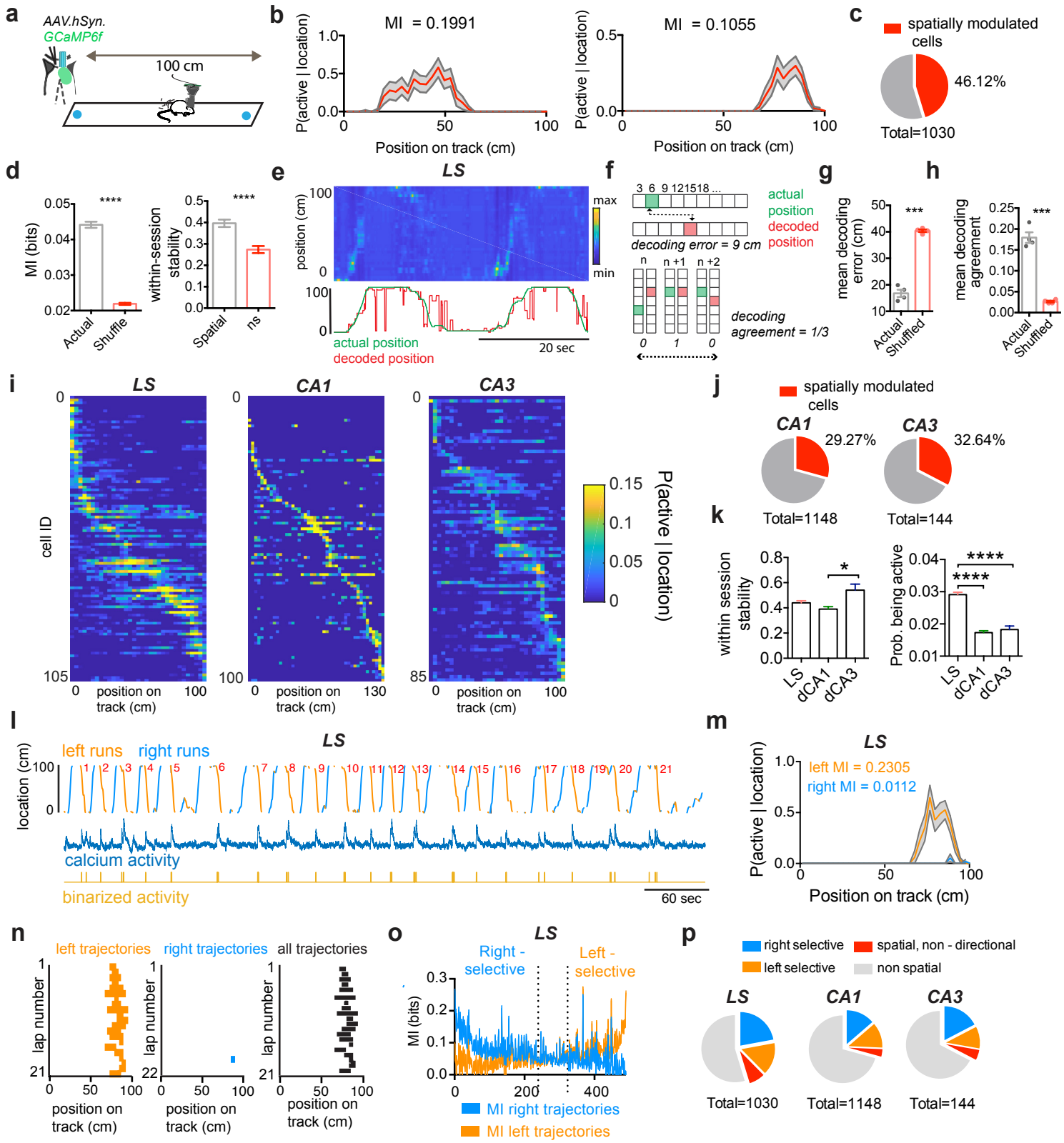
a
AAV.hSyn.
GCaMP6f
100 cm
b
MI = 0.1991
P(active | location)
Position on track (cm)
MI = 0.1055
c
spatially modulated cells
46.12%
Total=1030
d
MI (bits)
****
Actual
Shuffle
within-session stability
Spatial
ns
e
LS
position (cm)
max
min
actual position
decoded position
20 sec
f
actual position
decoded position
decoding error = 9 cm
decoding agreement = 1/3
g
mean decoding error (cm)
***
Actual
Shuffled
h
mean decoding agreement
i
LS
CA1
CA3
cell ID
position on track (cm)
P(active | location)
j
spatially modulated cells
CA1
29.27%
CA3
32.64%
Total=1148
Total=144
k
within session stability
Prob. being active
LS
dCA1
dCA3
l
LS
left runs
right runs
location (cm)
calcium activity
binarized activity
60 sec
m
LS
left MI = 0.2305
right MI = 0.0112
P(active | location)
Position on track (cm)
n
left trajectories
right trajectories
all trajectories
lap number
position on track (cm)
o
LS
Right - selective
Left - selective
MI (bits)
MI right trajectories
MI left trajectories
p
right selective
spatial, non - directional
left selective
non spatial
LS
CA1
CA3
Total=1030
Total=1148
Total=144

Figure 7

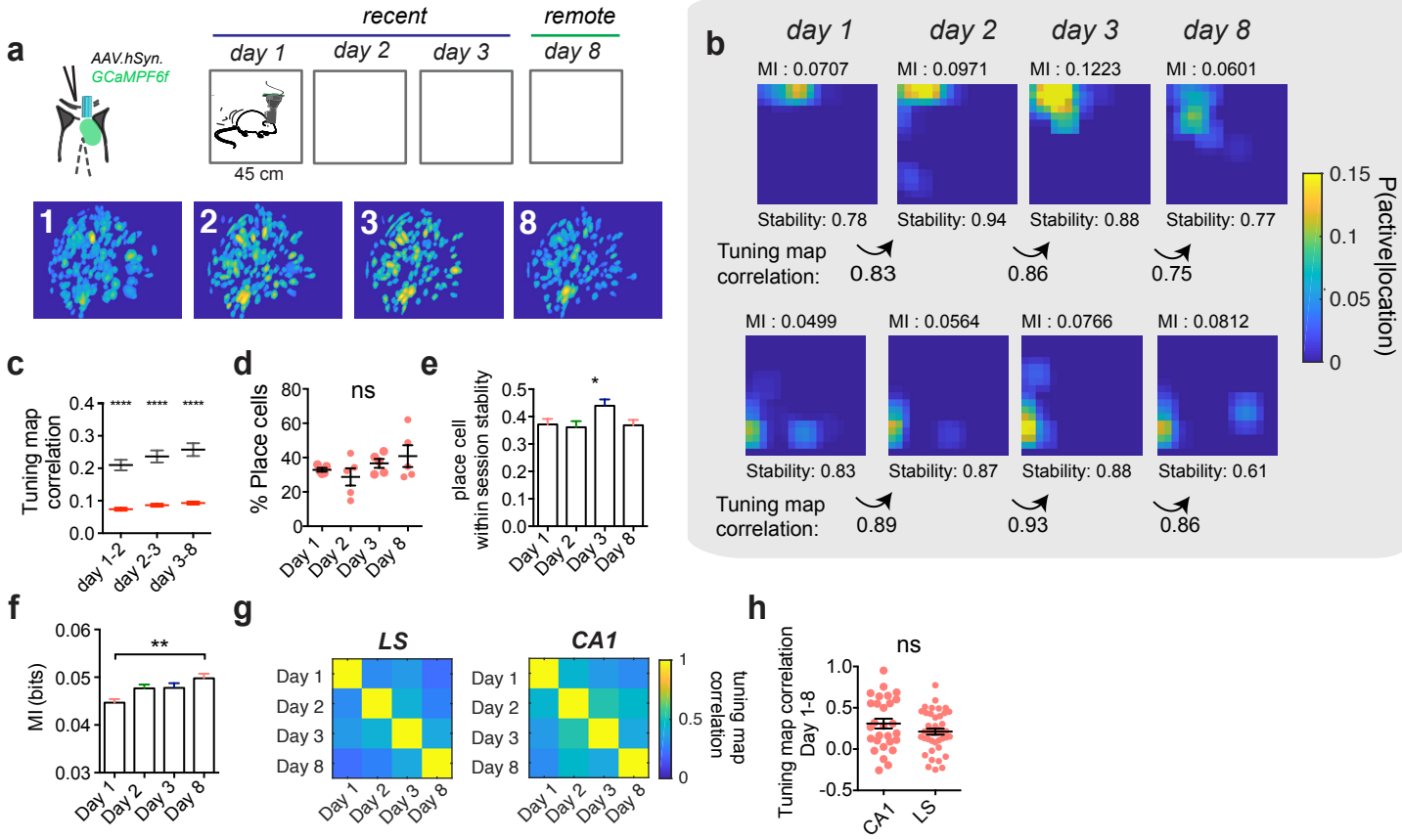
a
AAV.hSyn.
GCaMPF6f
recent
remote
day 1
day 2
day 3
day 8
45 cm
1
2
3
8
b
day 1
day 2
day 3
day 8
MI : 0.0707
MI : 0.0971
MI : 0.1223
MI : 0.0601
Stability: 0.78
Stability: 0.94
Stability: 0.88
Stability: 0.77
Tuning map correlation:
0.83
0.86
0.75
MI : 0.0499
MI : 0.0564
MI : 0.0766
MI : 0.0812
Stability: 0.83
Stability: 0.87
Stability: 0.88
Stability: 0.61
Tuning map correlation:
0.89
0.93
0.86
P(active|location)
0.15
0.1
0.05
0
c
Tuning map correlation
****
****
****
day 1-2
day 2-3
day 3-8
d
% Place cells
ns
Day 1
Day 2
Day 3
Day 8
e
place cell within session stability
*
Day 1
Day 2
Day 3
Day 8
f
MI (bits)
**
Day 1
Day 2
Day 3
Day 8
g
LS
CA1
Day 1
Day 2
Day 3
Day 8
tuning map correlation
h
Tuning map correlation Day 1-8
ns
CA1
LS